

Article

Targeting cytokinesis bridge proteins to kill high-CIN type tumors

Bingteng Xie^{a,b,c,d,1}, Xiaoling Liang^{a,b,c,d,1}, Wei Yue^{a,b,c,d,1}, Jihong Ma^{a,b,c}, Xinyu Li^a, Na Zhang^a, Pan Wang^a, Chang Liu^e, Xiaomeng Shi^f, Jie Qiao^{a,b,c,d}, Peng Zou^g, Mo Li^{a,b,c,d,*}

^a Center for Reproductive Medicine, Department of Obstetrics and Gynecology, Peking University Third Hospital, Beijing 100191, China

^b National Clinical Research Center for Obstetrics and Gynecology (Peking University Third Hospital), Beijing 100191, China

^c Key Laboratory of Assisted Reproduction (Peking University), Ministry of Education, Beijing 100191, China

^d Beijing Key Laboratory of Reproductive Endocrinology and Assisted Reproductive Technology (Peking University Third Hospital), Beijing 100191, China

^e Department of Anesthesiology, Peking University Third Hospital, Beijing, China

^f State Key Laboratory of Natural and Biomimetic Drugs, School of Pharmaceutical Science, Peking University, Beijing 100191, China

^g College of Chemistry and Molecular Engineering, Peking-Tsinghua Center for Life Sciences, PKU-IDG/McGovern Institute for Brain Research, Peking University, Beijing 100871, China



ARTICLE INFO

Article history:

Received 7 April 2021

Received in revised form 2 August 2021

Accepted 3 August 2021

Available online 17 September 2021

Keywords:

Cytokinesis bridge proteome

APEX2, High-CIN tumors

Micronuclei

cGAS

ABSTRACT

As a common feature of tumors, chromosomal instability (CIN) not only forces carcinomatous evolution, but also loads cancer cells with extra pressure through a robust imbalance of genome patterning that may be used for cancer treatment. Errors in cytokinesis increase CIN, so cytokinesis components are valuable targets for treating cancer. However, due to the short time span and confined space of cytokinesis bridges, profiling cytokinesis factors is challenging. Taking advantage of engineered ascorbate peroxidase (APEX2), we established a cytokinesis bridge-APEX reaction in living cells. A total of 218 cytokinesis bridge proteins were identified with high reliability. Knockdown of cytokinesis bridge genes generated micronuclei that activate the cGAS-pathway and cause apoptosis in cancer cells bearing high CIN rather than low CIN. Thus, our study proposes a strategy for killing high-CIN tumors regardless of tumor type, and provides a proteome resource of cytokinetic bridges for future research.

1. Introduction

Tumors are the leading lethal disease for humans. Scientists have investigated strategies for killing a wide range of tumors for decades. However, mounting evidence from high-throughput sequencing has revealed high heterogeneity and numerous cancer-associated mutations within tumors [1,2]. Data from systematic studies further demonstrate that various signals involved in multifaceted biological processes are affected by multiple tumor drivers [3–5], limiting the development of broad-spectrum treatments against tumors. All tumors have a significant hallmark of chromosomal instability (CIN) to different extents, characterized by changes in chromosomal structure or number [6–8]. Even a near-diploid cancer cell has been estimated to experience at least one genome doubling during tumorigenesis [9,10]. CIN promotes cancer evolution under selection pressure and is associated with poor prognoses, aggressive features, and clinical drug resistance [11–14]. However, CIN also endows cancer cells with a uniform and damaging state of stress through metabolic alterations, energy burden, and imbalance of gene expression patterning, which might be specifically targetable for

killing cancer [15–19]. Once beyond the tolerable limitation for stress, cancer cells collapse and die. Thus, exacerbating CIN may be an effective strategy for killing tumors. However, methods for elevating CIN to selectively kill cancer cells are largely unknown.

Cytokinesis defects affect ploidy by increasing CIN of cells [13,20]. With the innate traits of karyotypic complexity and CIN, cancer cells should be easily induced to break their viability by perturbing certain factor(s) in the cytokinesis regulatory network. RNAi-based selection for loss of function, cell imaging, and *in vitro* experiments have provided insights into genes involved in cytokinesis. These lines of work outline the intensive actions of cytoskeleton molecules and cell cycle engines, as well as energy metabolism factors at the end of mitosis [21–25]. However, unlike the other stages of the cell cycle that are well studied, the full picture of cytokinesis is still unknown mainly due to the confined space of the cytokinetic bridge that limits most experimental operations [25–27]. Also, the transient process of cytokinesis spans a very short portion of the cell cycle, increasing the challenge of acquiring comprehensive information throughout the cycle. This largely impedes mining of potential cytokinesis targets for anticancer strategies. Thus, a systemic

* Corresponding author at: Center for Reproductive Medicine, Department of Obstetrics and Gynecology, Peking University Third Hospital, Beijing 100191, China. E-mail address: limo@hsc.pku.edu.cn (M. Li).

¹ These authors contributed equally to this work.

proteome profile of the cytokinesis bridge especially *in situ* is imperative and valuable.

In this study, we aimed to decipher the proteome of the cytokinetic bridge and explore whether a broad range of cancer cells could be killed by inducing them to a higher state of CIN by targeting cytokinesis factors. Taking advantage of engineered ascorbate peroxidase (APEX2) technology [28–30], we established a cytokinesis bridge-APEX (CB-APEX) reaction to selectively biotinylate cytokinesis bridge proteins *in situ* with high spatial specificity. A total of 218 proteins were identified in the cytokinesis bridge, which are mainly involved in ‘microtubule binding’, ‘mitotic nuclear division’, ‘telomere maintenance’, and ‘secretory granule membrane’. Numerous cytokinesis bridge genes are highly expressed across many types of carcinoma. Intriguingly, knockdown of some cytokinesis bridge genes (e.g. PPP4C and TBCB) elevated cellular CIN, causing significant cytokinesis failure marked by micronuclei during cytokinesis in tumor cells bearing innate high-CIN rather than low-CIN. These micronuclei activated the cGAS-pathway and resulted in apoptosis in many types of clinical tumors from breast, ovarian, colorectal, and gastric cancer patients. Thus, our study proposes a strategy for killing a broad range of cancer cells bearing high-CIN regardless of tumor types, and provides a proteome resource of cytokinesis for future research.

2. Materials and methods

2.1. Ethics

All human materials used in this study were approved by the Medical Science Research Ethics Committee of Peking University Third Hospital (IRB00006761-M2019471). Signed informed consents were obtained from all patients who participated in the study. Mice care and handling were conducted in accordance with policies promulgated by the Ethics Committee of the Peking University Health Science Center.

2.2. Chemicals and antibodies

All chemicals were purchased from Sigma except for those specifically mentioned. Anti-AK2 (NBP1-33160), CDK4 (NBP1-31308), LMAN2 (NBP1-86768), PP4/PPP4C (NBP2-13802), and Ki67 (NB500-170) antibodies were purchased from Novus. Anti-HDGF (11344-1-AP), NME1 (11086-2-AP), PDIA3 (15967-1-AP), SEC61B (51020-2-AP), TBCB (15782-1-AP), TPT1 (10824-1-AP), TRIM28 (15202-1-AP), UBE2S (14115-1-AP), IRF3 (11312-1-AP), TMEM173/STING (19851-1-AP), and β -actin (66009-1-Ig) antibodies were purchased from Proteintech. Anti-Phospho-IRF-3 (Ser396) (29047), Phospho-STING (Ser366) (50907), Phospho-Histone H2A.X (Ser139) (2577), cGAS (15102), and Cleaved Caspase-3 (Asp175) (9664) antibodies were purchased from Cell Signaling Technology. Anti-Bax (6A7) (sc-23959) antibody was purchased from Santa Cruz Biotechnology. Anti-PSMD8 (ab246883), SLIRP (ab51523), and TAGLN2 (ab121146) antibodies were purchased from Abcam. Alexa Fluor® 555 streptavidin (S21381), HRP Streptavidin Protein (21127), anti-MRPS34 (PA5-59872), RPL28 (PA5-62192), TPM3 (720306) antibodies, FITC anti-alpha Tubulin Monoclonal antibody (MA1-19581), anti-alpha Tubulin Monoclonal antibody (A11126), Alexa Fluor™ 647 Phalloidin (A22287), Alexa Fluor™ 633 goat anti-mouse IgG (A-21126), Alexa Fluor™ 633 goat anti-Rabbit IgG (A-21071), Alexa Fluor™ 488 goat anti-mouse IgG (A-11001), Alexa Fluor™ 488 goat anti-Rabbit IgG (A-11008), HRP goat anti-mouse IgG (H+L) secondary antibody (32430), and HRP goat anti-rabbit IgG (H+L) secondary antibody (31466) were purchased from Thermo Fisher Scientific.

2.3. Plasmid construction

To guide APEX2 to cytokinesis bridges, APEX2 sequence was fused to the CDS/CDS fragment of cytokinesis candidate genes (CEP55, IN-

CENP, BIRC5, PDCD6IP, TSG101, CHMP1B, CHMP4C, VPS4B), and sub-cloned into pcDNA3 with the EGFP tag. To establish a stable cell line expressing BIRC5-APEX2-EGFP, the sequence of APEX2-EGFP was inserted into the endogenous *BIRC5* locus using the CRISPR/Cas9 system. The guide RNA for the *BIRC5* gene (CAGCTGGCTGCCATGGATTG) was designed at <https://zlab.bio/guide-design-resources>, and was cloned into the pSpCas9(BB) vector for co-expression with Cas9 (Addgene plasmid #62988). The donor plasmid contains the APEX2-EGFP sequence flanked by ~1,000-bp homologous arms of the *BIRC5* locus. To knock down the expression of target genes (AK2, CDK4, HDGF, LMAN2, MRPS34, NDUFA9, NME1, PDIA3, PPM1G, PPP4C, PSMD8, RPL28, SEC61B, SLIRP, TAGLN2, TBCB, TPM3, TPT1, TRIM28, UBE2S, and cGAS), the oligos encoding shRNA were cloned into pLKO.1 vector. Sequences of shRNAs are provided in Table S8.

2.4. Cell synchronization

HeLa cells were first synchronized to early S phase with the double thymidine block procedure. Briefly, when grown to ~40% confluence, cells were treated with 2 mM thymidine for 15 h, released for 9 h, and then blocked again with 2 mM thymidine for 15 h. After being washed out from the second thymidine block, cells were incubated with 0.1 μ g/ml nocodazole for 10 h. Arrested cells were synchronously released by extensive washing (three times) with warm Dulbecco’s Modified Eagle’s Medium (DMEM) containing biotin-phenol (BP) medium and were then allowed to progress for 60 min into cytokinesis. These cytokinesis cells were then used for the CB-APEX reaction.

2.5. APEX2-mediated biotinylation

Cells (~3 \times 10⁷ for each sample) stably expressing BIRC5-APEX2-EGFP were incubated with 500 μ M BP dissolved in DMEM at 37 °C under 5% CO₂ for 60 min. H₂O₂ was added to a final concentration of 1 mM for 1 min at room temperature to initiate the reaction. The reaction was quenched three times by replacing the medium with an equal volume of “quencher solution” (10 mM sodium ascorbate, 10 mM sodium azide, and 5 mM Trolox in DPBS). Cell pellets were immediately lysed in lysis buffer (50 mM Tris-HCl [pH 7.4], 150 mM NaCl, 0.5% SDS, 0.5% sodium deoxycholate, 1% Triton X-100, 1 \times protease inhibitor cocktail, 10 mM sodium azide, 10 mM sodium ascorbate, 5 mM Trolox, and 20 mM DTT). After gentle sonication, the lysates were cleared by centrifugation at 12,000 rpm for 5 min at 4 °C, and then ten times the volume of ice-cold methanol was added followed by precipitation at -80 °C for 6 h. Proteins were harvested by centrifugation at 4,000 rpm for 30 min at 4 °C, and then re-dissolved in 1% SDS RIPA buffer. In total, 4 mg protein of each sample (in 0.2% SDS RIPA buffer) was separately incubated with 150 μ L of streptavidin-coated magnetic bead slurry with rotation for 2 h at room temperature. The beads were subsequently washed twice with 1 mL of RIPA lysis buffer, once with 1 mL of 1 M KCl, once with 1 mL of 0.1 M Na₂CO₃, once with 1 mL of 2 M urea in 10 mM Tris-HCl (pH 8.0), and twice with 1 mL RIPA lysis buffer. Biotinylated proteins were then eluted by boiling the beads in 60 μ L of protein loading buffer supplemented with 20 mM DTT and 2 mM biotin.

2.6. Sample preparation and mass spectrometry

Protein samples for mass spectrometry were prepared according to a previous study [28]. In brief, biotinylated proteins eluted from streptavidin beads were run on SDS-PAGE. The gels were stained with Coomassie G-250 and destained with water. The lane of each sample was manually cut into seven gel bands. After in-gel digestion, a vacuum concentrator was used to completely dry the peptides. The seven gel fractions were combined into three injections. The dried peptides were reconstituted in 100 μ L of 0.1% formic acid and loaded on to C18 StageTips conditioned with 50 μ L of 50% acetonitrile/0.1% formic acid. The tips were washed twice with 50 μ L of 0.1% formic acid, and peptides

were eluted with 50% acetonitrile/0.1% formic acid, before drying in a vacuum concentrator.

A Q Exactive mass spectrometer (Thermo Scientific) coupled online to an Easy-nLC 1200 UPLC (Proxeon) was used for analysis. The extracted peptides were dissolved with 25 μ l of Solvent A (0.1% formic acid in water), and loaded to a homemade trap column (100 μ m \times 2 cm) packed with C18 reverse-phase resin (particle size, 3 μ m; pore size, 120 Å; SunChrom, USA) at a maximum pressure of 220 bar with 12 μ l of solvent A, then separated on a 150 μ m \times 15 cm silica microcolumn (homemade, particle size, 1.9 μ m; pore size, 120 Å; SunChrom, USA) with a gradient of 5–42% mobile phase B (80% acetonitrile and 0.1% formic acid) at a flow rate of 800 nl/min for 30 min. The gradient elution conditions (30 min) were: 5% to 15% mobile phase B for 3 min; 15% to 42% for 21 min; 42% to 95% for 1 min; 95% for 5 min. The MS analysis was performed in data-dependent acquisition (DDA) mode with full scans (*m/z* 300–1400) acquired using an Orbitrap mass analyzer at a mass resolution of 60,000. The most intense ions selected under top-speed mode were isolated in quadrupole with a 1.6 *m/z* window and fragmented by higher energy collisional dissociation (HCD) with a normalized collision energy of 27%, then detected in the Orbitrap at a mass resolution of 15,000. The automatic gain control (AGC Targets) for full MS was set to 3e6, and that for MS/MS was set to 5e4, with maximum ion injection times of 20 and 12 ms, respectively. The dynamic exclusion time was 15 s. Peptide match and isotope exclusion were enabled.

2.7. Protein identification

Raw files were searched against the human RefSeq protein database (2017/11/01) with Proteome Discoverer (Thermo Fisher Scientific, version 2.1) using the SEQUEST HT search engine with percolator. Mass tolerance for precursor ions was set to 20 ppm; mass tolerances of fragment ions were 0.05 Da for Q Exactive. Oxidation of methionine, carbamidomethylation of cysteine, and acetylation of protein N-terminal were included as variable modifications. A maximum of two missed cleavages was allowed. All assigned peptides were filtered with a 1% false discovery rate (FDR) at the peptide level. All identified peptides were quantified with peak areas derived from their intensity of MS1. The procedure was operated as: MS raw data were converted to the MS-platform independent mzXML format, and the spectral assignments from PD2.1 were then channeled through an in-house pipeline to construct extracted ion chromatogram (XIC) peaks with their corresponding intensity values included in mzXML data. The intensity based absolute quantification (iBAQ) algorithm was used to quantify proteins [31]. To normalize among loading samples, iBAQ value was converted to a fraction of total (FOT) - iBAQ value of each protein divided by the sum of all iBAQ values of all proteins in each sample. Thus, FOT number is a relative concentration for the protein in the total measurable proteome. For visualization, the FOT number was multiplied by 10⁵. Three replicates of reaction and control (in absence of H₂O₂, for nonspecific deduction) experiments were conducted. We only kept protein identifications with ≥ 2 unique peptides in at least one replicate, and positive FOT value in at least two replicates. Proteins with their mean FOT value in reaction groups twofold higher than those in control groups were screened out. Further, proteins with *p* values (FOT value in reaction groups vs. in control groups) < 0.05 were finally identified. Volcano plots were generated for visual representation of identified proteins using the R package ggplot2.

2.8. Bioinformatics analysis of cytokinesis bridge genes

Overall survival analysis used the database TCGA (The Cancer Genome Atlas Program, <https://www.cancer.gov/about-nci/organization/ccg/research/structural-genomics/tcga>). In total, 218 cytokinesis bridge genes and clinical tumor samples (9504 analyzable samples across 33 types of cancers, see Table S4) from the TCGA database were divided into four equal parts (bottom quartile, mid-low

quartile, mid-high quartile, and top quartile) based on the global expression level of the 218 cytokinesis bridge genes set. The global expression level was calculated by mean value of log₂ (transcripts per million + 1) of each gene in the set. Survival analysis was performed with the bottom quartile group (N=2,376, blue, low expression) and top quartile group (N=2,376, red, high expression) using Kaplan-Meier curves, which were run on Gene Expression Profiling Interactive Analysis 2 (GEPIA2) (<http://gepia2.cancer-pku.cn>) [32]. A log-rank test was used to compare the survival curves of the two groups, and a hazards ratio (HR) was calculated based on the Cox PH Model. For expression analysis of cytokinesis bridge genes in tumor patients and normal controls, the transcript expression levels of 218 genes in 8,881 tumor samples (27 analyzable cancer types) and 5361 paired normal tissue samples were extracted from the databases and run in the R package ggplot2. Mean values of gene expression medians in all tumor samples and fold change of tumor/normal samples were calculated. For analysis of genome alterations of 20 representative cytokinesis bridge genes, annotation of the mutations using Genome Nexus (by VEP with the canonical UniProt transcript) were standardized by <https://cbioportal.org/>. Copy number data sets within the portal were generated by the GISTIC or RAE algorithms. Both algorithms identify significantly altered regions of amplification or deletion of genes of interest across sets of patients. Both algorithms also generate putative gene/patient copy number specific calls, which are then input into the portal. Pathway enrichment and GO analysis of cytokinesis bridge proteins were conducted using the Web-based Gene Set Analysis Toolkit (WebGestalt, <http://www.webgestalt.org/>) and R-clusterProfiler. *p* values for the representative GO terms shown in the present study were adjusted with the Benjamini-Hochberg procedure [33].

2.9. Immunofluorescence and 3D reconstruction

Cells were fixed in 4% paraformaldehyde in PBS (pH 7.4) for 30 min followed by permeabilization in 0.5% Triton-X-100 for 25 min at room temperature. Then, samples were blocked with 1% BSA-supplemented PBS for 1 h and incubated with primary antibodies (1:200–1:500) at 4 °C overnight. After washing three times in PBS containing 0.1% Tween 20 and 0.01% Triton-X 100, the cells were incubated with an appropriate fluorescent secondary antibody for 1 h at room temperature. After washing three times, the cells were stained with Hoechst 33342 (10 μ g/ml) for 15 min. Finally, the samples were mounted on glass slides and observed under a confocal laser scanning microscope at 63x/1.40 (Carl Zeiss 710). Images for 3D reconstruction were obtained from Z-stack scanning at 0.25 μ m intervals capturing the entire cytokinesis bridge under a confocal microscope at 63x/1.40 (Carl Zeiss 880). After import of CZI files, different channels of BIRC5-APEX2-EGFP, biotinylated proteins, microtubules, and chromosomes were analyzed using the Imaris program (Bitplane, Belfast, United Kingdom) [34,35]. 3D surface rendering was carried out to obtain a 3D reconstruction of cytokinesis bridge components in the bridge of dividing cells. Imaris Volume-Specific Values was used for volume calculation.

2.10. Cell culture and live imaging

HeLa, MCF7, and MRC5 cells were cultured in DMEM with 10% fetal bovine serum (FBS). MCF-10A cells were cultured in DMEM/Nutrient Mixture F-12 with 5% FBS, 1 \times ITS, 0.02 μ g/ml EGF, 0.5 μ g/ml hydrocortisone, and 0.1 μ g/ml cholera toxin. For live imaging, cells were grown on imaging culture dishes (NEST, 801001) and observed in UltraVIEW VoX (PerkinElmer) live cell workstation at 37 °C with 5% CO₂ for indicated time. Images were analyzed by Volocity (Universal 3D Image).

2.11. Isolation and culture of primary tumor cells

Fresh tumor samples were harvested from patients with diverse types of cancers. Detailed information of the tumor samples is pro-

vided in Table S5. After washing with PBS, 0.1 and 0.2 cm³ of the tumor specimen was cut off and mechanically disintegrated into pieces smaller than 1 mm³ using scalpels followed by digestion in 1 × collagenase/hyaluronidase buffer (STEMCELL Technologies) at 37 °C with agitation for 6 h. Further digestion was performed by gentle pipetting in trypsin (0.25%) and then in a solution of dispase (5 units/ml) and DNase I (0.05 mg/ml; STEMCELL Technologies) for 5–10 min. By filtration through a 40-μm filter, single-cell suspensions were obtained. These cells were then seeded at a density of 0.5–1 × 10⁵/well onto 6-well plates coated with collagen I and cultured for 36–72 h. Culture medium was composed of DMEM:F12 supplemented with 5% FBS, penicillin/streptomycin (1%), gentamycin (0.2%), EGF (10 ng/ml), adenine (20 μg/ml), cholera toxin (10 ng/ml), HEPES (15 mM), insulin (5 μg/ml), hydrocortisone (0.32 μg/ml), and ROCK inhibitor (5 μM). After stable adhesion, cells could be further cultured and passaged or frozen in FBS/DMSO (9:1) with 5 μM ROCK inhibitor in liquid nitrogen.

2.12. shRNA lentivirus generation and shRNA knockdown

For shRNA lentivirus generation, shRNA sequences were designed using “shRNAs for Individual Genes” purchased from Sigma Aldrich. The sequences of scramble and gene targeting shRNA were provided in “Oligonucleotides” above. The pLKO.1 plasmid comprising shRNA was cotransfected with the packaging plasmids (psPAX2 and pMD2.G) into HEK293T cells using Lipofectamine 3000™ according to the manufacturer’s protocol. Six hours after transfection, the cells were washed and changed with fresh growth culture media and incubated for another 48 h. Then the culture media containing viral particles were harvested and centrifuged at 3000 × g for 5 min to remove the cell debris and filtered by a 0.45 μm filter. The viral supernatant was further concentrated with a Centricon Plus-20 Centrifugal Filter at 4,000 × g. The concentrated lentivirus supernatant was aliquoted and kept at -80 °C before use. To knock down genes of interest in HeLa cells, 10⁵ HeLa cells were seeded onto 6-well plates and incubated at 37 °C with 5% CO₂ until reaching 30–40% confluence. The concentrated viral supernatant was added into the culture medium at a multiplicity of infection (MOI) of 20. After 72 h, puromycin was added to the medium at 1 μg/ml for stable knockdown selection.

2.13. DNA preparation and whole genome sequencing (WGS)

Genomic DNA of cells and tumor samples was extracted and purified using the DNeasy Blood & Tissue Kit (Qiagen, 69504) according to the standard protocol. DNA quality was assessed by gel electrophoresis and a Qubit® 2.0 Fluorometer (Life Technologies, CA, USA). A total of 1 μg of genomic DNA per sample was used for library construction with TruSeq DNA Sample Preparation Guide (Illumina, 15026486 Rev.C). Qualified DNA libraries were sequenced using Illumina Whole Genome Sequencing Service with Illumina HiSeq X (10X, ~30 GB/sample) at the Core Genomic Facility of Beijing Annoroad Genomics. All data were aligned to hg38 with BWA (Burrows-Wheeler Alignment tool) [36], arranged with SAMtools (Sequence Alignment/Map tool) [37], marked with Picard (<http://broadinstitute.github.io/picard/>), and locally aligned with GATK (Genome Analysis Toolkit) [38]. Variants were annotated using ANNOVAR tool (Annotate Variation) [39].

2.14. Chromosomal instability (CIN) assay

CIN assay was performed according to previous studies in which the weighted-genomic integrity index (wGII) was calculated as a proxy for CIN level [40,41]. For each sample and each of the 22 autosomal chromosomes, the percentages of gained and lost genomic material were calculated relative to the ploidy of the sample. The wGII score of a sample was defined as the average of this percentage value over the 22 autosomal chromosomes. To estimate somatic copy number variation, R package HMMcopy [42] and software package CNVkit [43] were

used to call copy numbers. Correlation between wGIIs from HMMcopy and CNVkit was assessed using the R package stats. For HMMcopy, the genome was divided into fixed 1 kb bins, and GC content and average mappability for bins were extracted from the genome. Read counts for bins of each sample were extracted from BAM files and corrected by GC content and mappability. After segmentation, segments of specific copy number variation events were classified into six states including homozygous deletion (HOMD), heterozygous deletion (HETD), neutral change (NEUT), gain of chromosome (GAIN), amplification event (AMPL), and high level amplification (HLAMP), using the Hidden Markov Model [44]. We used matched Tumor-Normal model for paired knockdown-control HeLa cells, and used Tumor only model for patient tumor samples in HMMcopy. CNVkit version 0.9.7 was used with default parameter on paired knockdown-control HeLa cells sequencing data.

2.15. Cell proliferation assay by xCELLigence system

Cell proliferation was assessed using the xCELLigence RTCA system (Acea Bioscience, San Diego, CA, USA, distributed by Roche Diagnostics) that allows long-term monitoring of live cells in a noninvasive manner [45,46]. In brief, 5000–10,000 cells were seeded in each well of E-16-well plates (Roche). Cell proliferation was monitored for 40–70 h at 37 °C in the incubator. Microelectrodes on the bottom of plates were used to detect impedance changes proportional to the number of adherent cells. The impedance value of each well was automatically recorded by Real-Time Cell Analyzer (RTCA) software. Two parallel wells were included for each sample in one replicate, and three independent replicates were conducted.

2.16. Patient-derived xenograft (PDX) model

Before implantation, necrotic areas of tumor specimens were removed as extensively as possible using sterile scissors. In total, 8–10 mm³ of tumor tissue was subcutaneously implanted into the flanks of 5- to 6-week-old NOD-SCID mice for the first generation of tumor growth, followed by weekly measurement of tumor volume with calipers. When tumor volume reached 800–2,000 mm³, the mice were sacrificed and the tumor was removed. The fresh tumor was cut into small pieces (4–8 mm³) and re-implanted into the flanks of 5- to 6-week-old BALB/c Nude mice for the second generation of tumor growth. When the tumor size reached 200–250 mm³, 5 × 10⁷ copies of gene targeting shRNA lentivirus or scramble shRNA lentivirus was injected into the tumor. The tumor growth was monitored for 40–60 days when the volume reached an ethical limitation of around 2,000 mm³. Each group included six mice. Tumor volume was calculated using the formula: (shortest diameter)² × longest diameter × 0.5.

2.17. Western blot

Total protein was extracted from cell lysate by RIPA buffer. Protein samples were separated by sodium dodecyl sulfate polyacrylamide gel electrophoresis (SDS-PAGE) and then electrically transferred to polyvinylidene fluoride membranes. Following transfer, the membranes were blocked in TBST containing 5% skim milk for 2 h, followed by incubation with primary antibodies (1:500–1:1000 dilution) overnight at 4 °C. After washing in TBST three times, the membranes were incubated at 37 °C for 1 h with a 1:1000 dilution of HRP-conjugated secondary antibody. For biotin labeled proteins, streptavidin-HRP conjugate was used. Finally, protein bands were visualized using an enhanced chemiluminescence detection system (Amersham Biosciences).

2.18. Histological staining

Histological staining was performed at the Immunohistochemistry Core of the Peking University Third Hospital. Tissues were fixed in 10% neutral-buffered formalin solution for 12–16 h and gradually transferred

to 70% ethanol. After embedding in paraffin, the tissues were cut in 5 μm sections on polylysine-coated slides and stained with hematoxylin and eosin, or indicated antibodies. The dilutions of anti-Ki67 and anti-cleaved Caspase 3 were 1:200 and 1:500, respectively. Images were taken and analyzed using an Olympus BX51 microscope and DP73 CCD photographic system.

2.19. cGAMP ELISA

cGAMP level was measured with 2',3'-Cyclic GAMP Enzyme Immunoassay Kit (Arbor Assay, K067-H1). In total, 5×10^6 cells were harvested, washed with PBS and lysed in 500 μl RIPA Lysis buffer (Pierce, 89900) on ice for 20 min. Then the samples were centrifuged at $1000 \times g$ at 4 $^\circ\text{C}$ for 15 min, and the supernatant was used to measure cGAMP concentration according to the manufacturer's protocol.

2.20. RT-qPCR

The total RNA of tumor cells was extracted by TRIzol reagent (Gibco, 15596026) and the cDNA was synthesized by RevertAid RT Reverse Transcription Kit (Thermo, K1691). RT-qPCR was carried out on the StepOnePlus system (ABI) by PowerUpTM SYBRTM Green Master Mix (Thermo, A25742). Conditions of RT-qPCR were 95 $^\circ\text{C}$ for 2 min; 95 $^\circ\text{C}$ for 3 sec and 60 $^\circ\text{C}$ for 30 sec for 40 cycles. Expression levels of target genes were normalized to the expression of the housekeeping gene GAPDH. The relative mRNA expression level was calculated through the comparative cycle threshold method ($2^{-\Delta\Delta\text{Ct}}$).

2.21. Flow cytometry

Tumors cells were washed with PBS, trypsinized, and centrifuged at 1500 rpm for 3 min. Then the cells were washed three times with 1% BSA in PBS at 1,500 rpm for 3 min followed by fixation in 70% ethanol at 4 $^\circ\text{C}$ overnight. The fixed cells were washed with ice-cold PBS twice and incubated with RNaseA (50 $\mu\text{g}/\text{ml}$) at 37 $^\circ\text{C}$ for 30 min. After staining with PI (10 $\mu\text{g}/\text{ml}$) for 30 min, the samples were processed through an Attune NxT flow cytometer (Life Technologies) and the data were analyzed using FlowJo software.

2.22. Statistical analyses

All experiments were performed in triplicate unless indicated otherwise. Means and standard deviations were plotted. Student's *t*-test was used for statistical analyses. $P < 0.05$ (*) was considered statistically significant. Statistical details are included in figure legends.

2.23. Data and code accessibility

All raw files and search results for mass spectrometry of cytokinesis bridge proteomics have been deposited in ProteomeXchange via iProX (www.iprox.org) with the identification No. PXD020754 (for ProteomeXchange) and IPX0002396000 (for iProX). Whole genome sequencing (WGS) data of HeLa cells, patient tumor samples, and immortalized cell lines reported in this study have been deposited in the genome sequence archive of Beijing Institute of Genomics, Chinese Academy of Sciences, Beijing, China (gsa.big.ac.cn, accession no. PR-JCA003199).

3. Results

3.1. Targeting APEX2 into cytokinetic bridges

Given the rapid and dynamic process of cytokinesis, a prompt reaction is required in living cells. APEX2, a genetically encoded protein tag, has emerged as an efficient tool for proximity-dependent protein labeling at specific subcellular regions of interest within living cells

[28–30,47]. Upon addition of hydrogen peroxide (H_2O_2) for 1 min to cells preloaded with the biotin-phenol (BP) substrate, APEX2 generates biotin-phenoxy radicals that covalently tag proximal endogenous proteins [48]. In this study, we aimed to target the peroxidase and establish a reaction specifically within cytokinetic bridges of living cells. We started with fusing APEX2-EGFP to eight candidate proteins or domains predicted to be localized in the cytokinetic bridge [22,26] (Fig. S1a). Among these, four candidates showed relatively specific localization in the cytokinetic bridge of HeLa cells, including CEP55-APEX2-EGFP, BIRC5-APEX2-EGFP, CHMP1B-APEX2-EGFP, and PDCD6IP-APEX2-EGFP. Only BIRC5-APEX2-EGFP was retained exclusively in the bridge during cytokinesis (Figs. 1a, S1b). When we initiated the CB-APEX reaction by H_2O_2 , only BIRC5-APEX2-EGFP among the four candidates triggered the reaction precisely in the bridge (Figs. 1b, S1c). To achieve stable expression, we established BIRC5-APEX2-EGFP knockin HeLa cells. Consistently, the CB-APEX reaction was successful in the stable cell line (Fig. 1c), and was thus used for subsequent experiments.

We used 3D reconstruction in the Imaris program based on a series of high-resolution scans of the cytokinetic bridge to examine the reaction details in these cells. During cytokinesis, BIRC5-APEX2-EGFP (colored in green) was specifically targeted to the center of the cytokinetic bridge, which was attached by two bundles of microtubules (colored in cyan) linked to the segregated chromosomes. Accordingly, the CB-APEX reaction (colored in transparent red) occurred precisely at and around BIRC5-APEX2-EGFP without any nonspecific reaction in the whole cell (Fig. 1d). The volumes of the CB-APEX reaction surrounding BIRC5-APEX2-EGFP are shown in Fig. 1e. The dynamics of APEX2 fusion throughout the cell cycle were monitored by live cell imaging. In particular, BIRC5-APEX2-EGFP was exclusively targeted at the cytokinesis bridge during cell division. No non-specific signal was observed during the full cell cycle except for a weak distribution around the nuclear envelope after nuclear envelope breakdown (NEBD) (Fig. 1f, Video S1). The dynamic intensities of BIRC5-APEX2-EGFP in the cell cycle are summarized in Fig. 1g. These results suggest that the modified APEX2 can potentially be used for our CB-APEX reaction.

3.2. Proteome capture of cytokinesis bridge proteins and their association with clinical tumors

As cytokinesis spans a short interval during the full cell cycle, we strictly synchronized the cells and performed the CB-APEX reaction as outlined in Fig. 2a. After 1 min, the reaction was quenched and cells were lysed immediately. The lysate was incubated with streptavidin-coated magnetic beads and precipitated biotinylated proteins were analyzed with gel electrophoresis. As shown in Fig. 2b, BIRC5-APEX2-EGFP biotinylated a mass of proteins in a banding pattern, while few biotinylated proteins were observed in control samples omitting H_2O_2 , BP, or APEX2, meaning a successful proteomic capture in our system. Next, we generated proteomic data by nano LC-MS/MS (liquid chromatography tandem mass spectrometry). Three biological replicates were performed for CB-APEX reaction groups and control groups (without H_2O_2 , used for nonspecific deduction). Box plot and correlation analysis of MS data showed qualified protein abundance and replicate consistency (Pearson's correlation coefficient, 0.87–0.92) in both control and reaction groups (Fig. S2a, S2b). A total of 1552 proteins were detected in the reaction groups (Table S1). The average quantitative values of 459 proteins were twofold higher than those in control groups (Table S2). Of these, 218 proteins significantly enriched with p values < 0.05 were identified (Fig. 2c, Table S3). To confirm the specificity of the proteomic list, we aligned the 218 proteins in alphabetical order and spot checked them every tenth protein, for a total of $218/10 \approx 21$ (10th, 20th, 30th, ..., 210th) proteins, in an unbiased manner. Among the 21 proteins, 18 were definitely localized at the cytokinetic bridge in dividing cells (Fig. 2d), meaning that the positive rate of our list is around 85.7%. The 218 proteins are involved in 'microtubule binding', 'mitotic nuclear division',

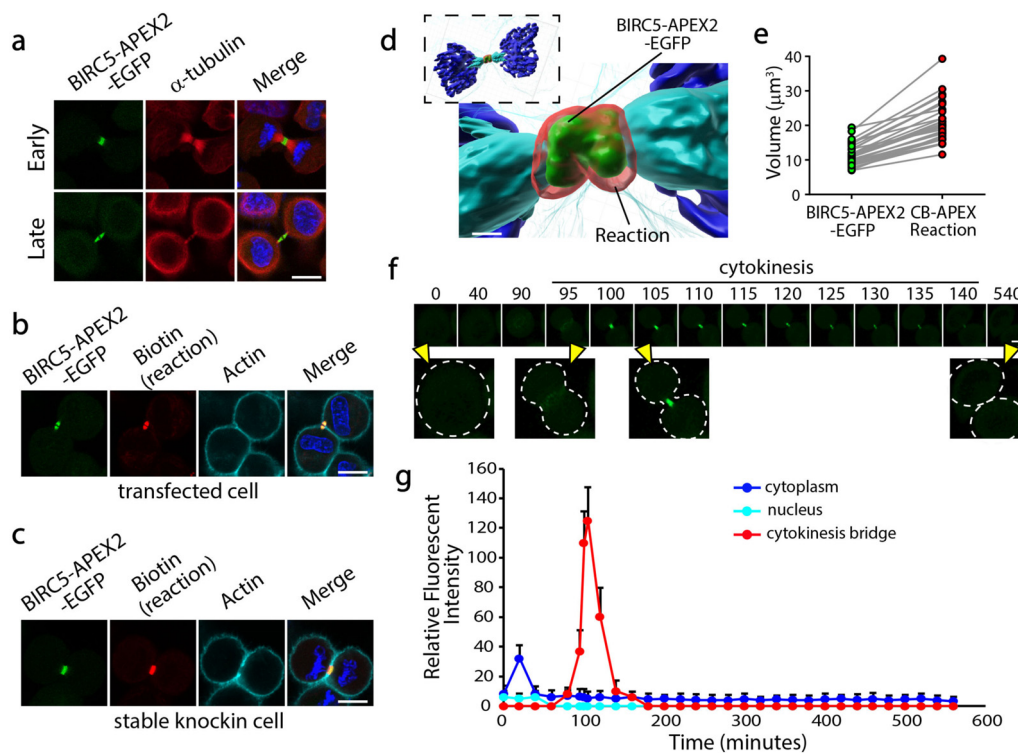


Fig. 1. APEX2 Targeting to the cytokinetic bridge. (a) Subcellular localization of BIRC5-APEX2-EGFP during cytokinesis in HeLa cells. APEX2 was fused to BIRC5 and EGFP followed by transfection and fluorescence detection of BIRC5-APEX2-EGFP (green), α -tubulin (red), and DNA (blue). Both early and late stages of cytokinesis are shown. (b) CB-APEX reaction in BIRC5-APEX2-EGFP transfected HeLa cells was triggered by biotin-phenol (BP) and H_2O_2 . The captured proteins labeled by biotin were stained in red, while cell borders were outlined by staining against actin in cyan. (c) CB-APEX reaction in HeLa cells stably expressing BIRC5-APEX2-EGFP. APEX2-EGFP knockin to the loci of *BIRC5* was accomplished using CRISPR-Cas9, forming cells stably expressing BIRC5-APEX2-EGFP for the CB-APEX reaction. The reaction pattern is consistent with that in (b). This cell line was used for subsequent experiments. Scale bar, 10 μ m. (d) 3D reconstruction of BIRC5-APEX2-EGFP in the cytokinesis bridge. Cells under the CB-APEX reaction were fixed and high-resolution scanned followed by 3D reconstruction with Imaris. The reconstructed BIRC5-APEX2-EGFP, reaction-captured proteins, microtubule bundles, and segregating chromosomes in the bridge were colored in green, transparent red, cyan, and blue, respectively. Note BIRC5-APEX2-EGFP was completely surrounded by the reaction-captured proteins. Scale bar, 1 μ m. (e) Volumes of BIRC5-APEX2-EGFP and reaction-captured proteins were calculated by Imaris Volume-Specific Values. Thirty cells from three independent replicates were summarized. The median volumes of BIRC5-APEX2-EGFP and reaction-captured proteins were 11.6 and 21.0 μ m³, respectively. (f) Live imaging of cells stably expressing BIRC5-APEX2-EGFP. The dynamic translocation of BIRC5-APEX2-EGFP was monitored by real time imaging for 540 min that covers at least a full round of the cell cycle. BIRC5-APEX2-EGFP exhibited specific localization in the cytokinetic bridge. Enlarged images denoted by yellow arrowheads are key time points of interphase, cytokinesis initiation, mid-cytokinesis, and cytokinesis completion. Dashed circles indicate cell outlines. Scale bar, 10 μ m. (g) Fluorescence kinetics of BIRC5-APEX2-EGFP during the cell cycle. Relative fluorescence intensities of BIRC5-APEX2-EGFP in the cytoplasm, nucleus, and cytokinesis bridge were separately recorded. Error bars, mean \pm SD. At least 30 cells in each group from three independent repeats were examined.

‘telomere maintenance’, ‘secretory granule membrane’, etc. (Fig. S2c). Several proteins, including ARF1 and MRPS34, which are known to be localized on the Golgi apparatus or mitochondria in interphase cells, were also found in our cytokinesis bridge list. We immunostained the proteins in dividing cells and confirmed their presence in the cytokinesis bridge (Fig. S2d). This finding implies certain new functions of these proteins during cytokinesis that are worth investigating in the future.

To identify the association between cytokinesis bridge proteins and cancers, we mapped all 218 candidates to the TCGA and GTEx databases, which store patients’ genomic information of different types of cancers, including breast cancer, cholangiocarcinoma, ovarian cancer, brain glioma, colon tumors, etc., as well as the paired normal controls [49,50]. Across the database of 33 available types of common cancers (Table S4), we first compared the overall survival status based on the expression of the 218 genes. Cancer patients ($n=2,376$) with high expression of these 218 genes have significantly shorter survival time than those ($n=2376$) who had low expression of these 218 genes (Fig. 2e). Moreover, we analyzed the mRNA expression levels of the 218 candidates in the databases according to two principles: 1, the expression of the gene in tumors is higher (\log_2 [fold change] >0.5) than that in the paired normal controls; and 2, the expression level (normalized transcript-level expression) of the gene is high in tumor tissue.

A series of genes were thus filtered out, and the Top 20 candidates (that are potentially most required for cytokinesis in tumor cells rather than in normal cells) were: AK2, CDK4, HDGF, LMAN2, MRPS34, ND-UF9, NME1, PDIA3, PPM1G, PPP4C, PSMD8, RPL28, SEC61B, SLIRP, TAGLN2, TBCB, TPM3, TPT1, TRIM28, and UBE2S (Figs. 2f and S3 show their subcellular localizations). The individual expression status of the 20 genes across diverse tumor types such as adrenocortical carcinoma (ACC), bladder urothelial carcinoma (BLCA), breast invasive carcinoma (BRCA), cervical squamous cell carcinoma and endocervical adenocarcinoma (CESC), etc., are displayed in Fig. 2g, showing that all genes were highly expressed in most of the tumor types. The analysis of genomic alterations showed that the Top 20 candidates have an obvious trend of amplifications but not deletions, further confirming the mRNA expression status above (Fig. 2h). These data suggest that the cytokinesis bridge proteins tend to be highly expressed in tumor tissues, and they could potentially be candidates to target for elevating CIN of cancer cells.

3.3. CIN elevation by knockdown of candidate cytokinesis bridge genes

Next, we wanted to know whether cellular CIN can be elevated by manipulating these cytokinesis bridge factors. The top 20 candidates

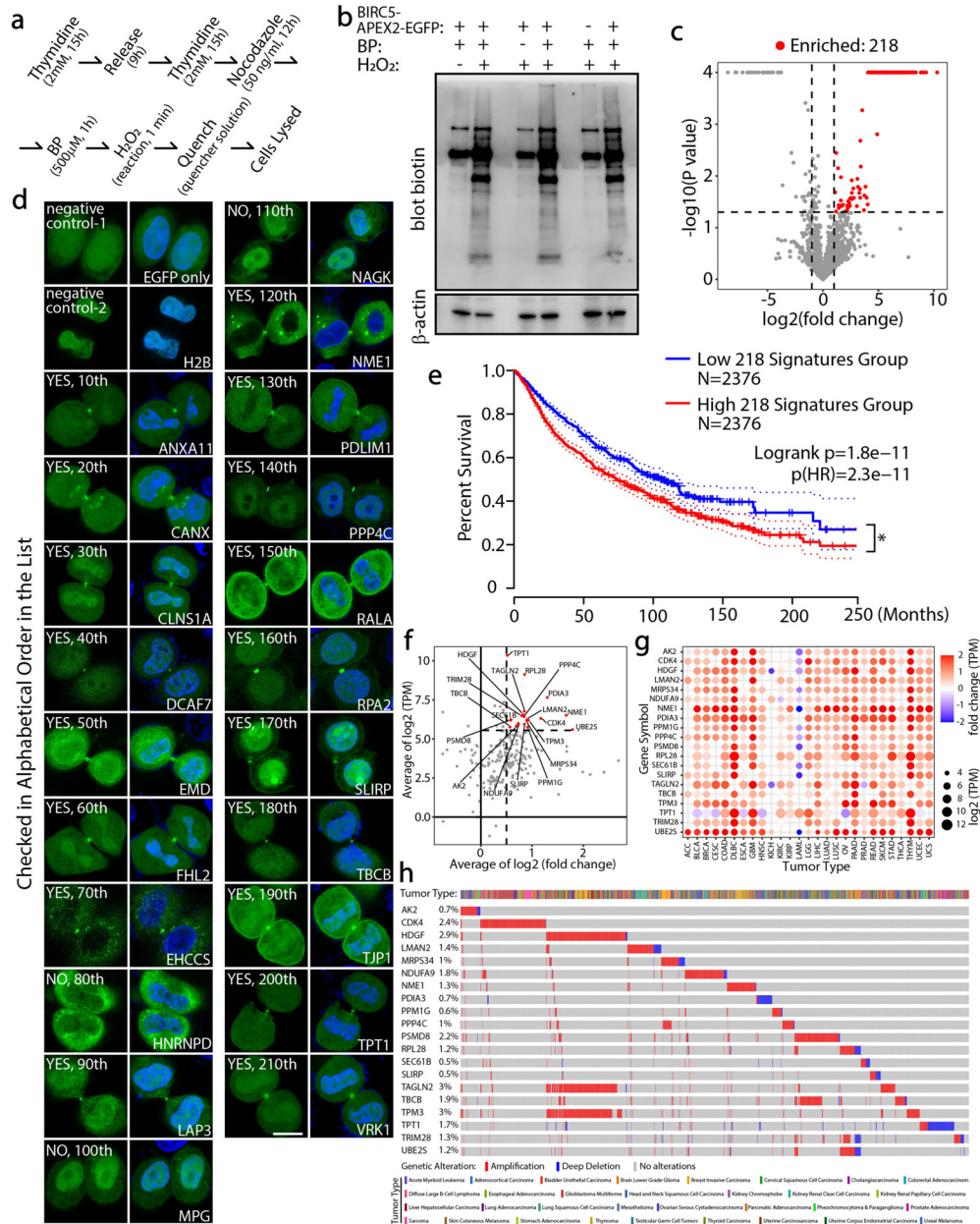


Fig. 2. CB-APEX reaction and proteomics analysis. (a) Flow diagram of CB-APEX reaction. HeLa cells stably expressing BIRC5-APEX2-EGFP were synchronized by two rounds of thymidine and one round of nocodazole followed by BP addition. The reaction was promptly triggered by H₂O₂ for 1 min. After reaction quenching, cells were immediately lysed for subsequent experiments. (b) SDS-PAGE of cell lysates from CB-APEX reaction. Cell lysates (from a) were incubated with streptavidin-coated magnetic beads and the precipitated biotinylated proteins were subjected to SDS electrophoresis for western blot against biotin. Reactions in the absence of H₂O₂, BP, or APEX2 (in BIRC5-EGFP expressing cells) were negative controls. β -actin was used as a loading control. (c) Volcano plot analysis of differentially expressed proteins between reaction and control groups. Proteins in reaction groups that were twofold higher than those in control groups are cut off by the dashed line. A total of 218 proteins that were significantly enriched with p values < 0.05 are labeled in red. (d) Immunofluorescence staining confirmation of alphabetically ordered candidates in the proteomic list. Every tenth candidate (10th, 20th, 30th, ..., 200th, 210th) of the 218 proteins in alphabetical order were selected for confirmation without subjective bias. Protein-EGFP coding plasmids were constructed and transfected into HeLa cells followed by immunofluorescent staining. Eighteen out of the 21 proteins were cytokinesis bridge localization positive, indicated by “YES”. Scale bar, 10 μ m. (e) An overall survival analysis of cancer patients in the public TCGA database who had relatively high expression of 218 cytokinesis bridge genes (N=2,376, red) versus cancer patients who had relatively low expression of 218 cytokinesis bridge genes (N=2,376, blue). Logrank $p=1.8e-11$; $p(HR)=2.3e-11$. Dotted line dots 95% confidence interval. (f) Top 20 candidates were screened from 218 cytokinesis bridge genes cut off by higher transcript expression in tumors than in the paired normal controls (\log_2 [fold change] > 0.5 , vertical dashed line), combined with the cut off by high transcript expression (normalized, horizontal dashed line) in tumor tissue *per se*. TPM, transcripts per million. (g) The individual expression levels of the top 20 candidates across diverse cancer types. The color schema from blue to red represents \log_2 (fold change) of gene TPM from low to high, respectively. Dot size indicates \log_2 value of TPM. (h) The analysis of genomic alterations of the top 20 candidates in diverse cancer types. All the genes (except TPT1) show an obvious trend of amplification rather than deletion in multiple types of cancer. The percentage denotes the rate of cancer patients carrying genetic alteration of cytokinesis gene among all cancer patients in the database. Color barcodes denote different cancer types.

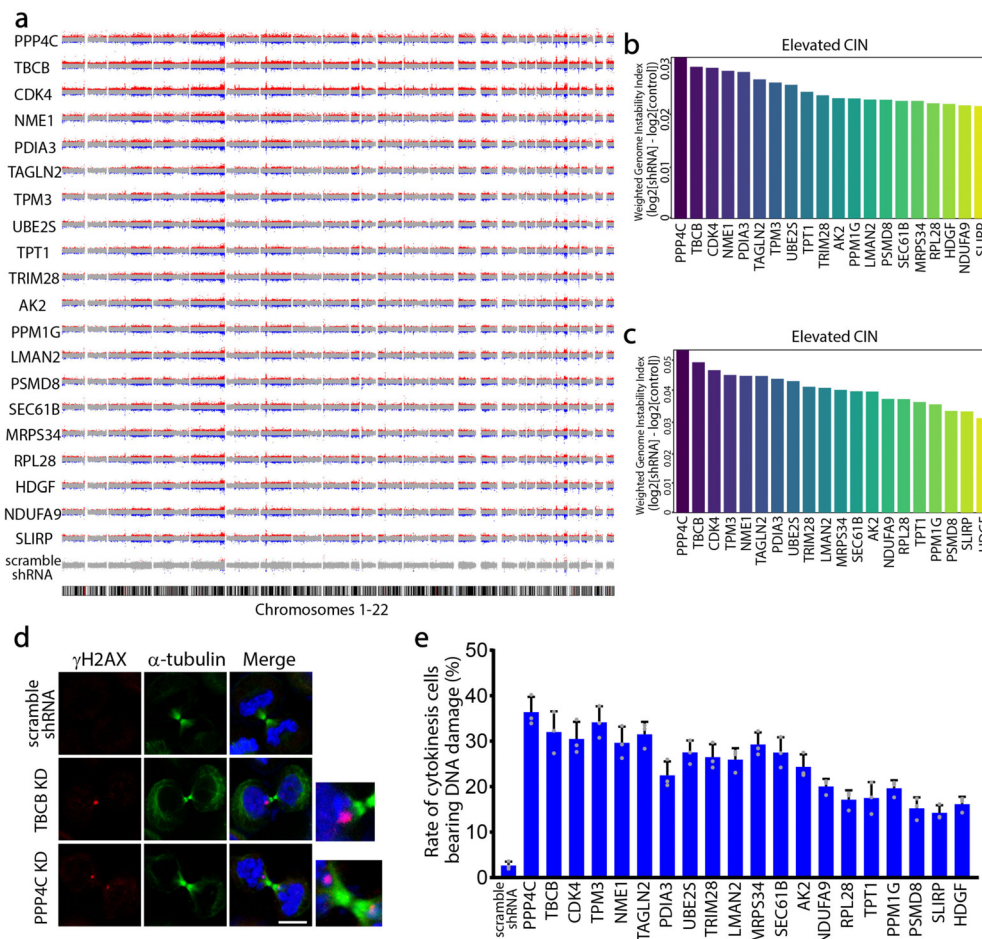


Fig. 3. Knockdown of cytokinesis bridge genes for CIN elevation. (a) CIN level of HeLa cells upon knockdown of cytokinesis bridge genes of interest was assessed using the weighted-genomic integrity index (wGII). Fold change of copy number in knockdown cells versus control cells was calculated in HMMcopy. Log₂ of the fold change >1 was labeled in red, while < -1 was labeled in blue. Individual data points denote log₂ ratios plotted to corresponding chromosomal location. (b) Extent of CIN elevation induced by knockdown of cytokinesis bridge genes were summarized from (a), and ranked in descending order. (c) Extent of CIN elevation induced by knockdown of cytokinesis bridge genes were calculated and summarized from the CNVkit program, and ranked in descending order. (d) DNA damage in cytokinesis cells upon knockdown of cytokinesis bridge genes. HeLa cells with or without knockdown of cytokinesis bridge genes were fixed during cytokinesis and stained against DNA damage marker γ H2AX. Scale bar, 10 μ m. (e) Rate of cytokinesis cells bearing DNA damage. The percentages of cells bearing DNA damage in different cytokinesis bridge gene knockdown groups were summarized. Error bars, mean \pm SD. At least 100 cells in each group from three independent repeats were examined.

above were individually knocked down by shRNA in HeLa cells (Fig. S4a) followed by whole genome sequencing (WGS) at a coverage depth of 10X (~30 GB raw data/sample, see deposited data). The CIN of cells treated by scramble or gene targeting shRNA was then assessed by the weighted-genomic integrity index (wGII) as a proxy for CIN level using HMMcopy and CNVkit [40–43,51]. Each assessment method generated a ranked list showing how much the gene knockdown raised cellular CIN (by $\log_2[\text{shRNA}] - \log_2[\text{control}]$) (Fig. 3a–c), and the two methods were highly consistent (Fig. S4b). All the individual knockdowns of 20 genes raised CIN to different extents. PPP4C and TBCB were the top 2 in both of the lists (Fig. 3b, 3c). Knockdown of either PPP4C or TBCB generated obvious variations of copy number in global chromosomes compared to the control cell without knockdown (Fig. 3a). The cytokinesis dysfunction-induced CIN is usually caused by structural chromosome aberrations originating from DNA damage [52]. We therefore detected the status of DNA damage in cytokinesis cells upon knocking down cytokinetic bridge genes. Knockdown of these cytokinetic bridge genes, especially PPP4C and TBCB, resulted in obvious DNA damages in the chromosome(s) close to the cytokinesis bridge compared to the control cells treated with scramble shRNA (Fig. 3d), meaning that cytokinesis errors could give rise to damages or breaks in the chromosomes in or

near the cytokinetic bridge during cell division. The rates of dividing cells bearing DNA damage in different knockdown groups are summarized in Fig. 3e. These results suggest that manipulation of cytokinetic bridge genes, especially PPP4C and TBCB, can elevate cellular CIN.

3.4. Knockdown of cytokinesis bridge genes PPP4C and TBCB suppresses cancer cell proliferation of diverse high-CIN tumors

Given their effect on increasing CIN, we explored whether depletion of PPP4C and TBCB would suppress the proliferation of multiple types of tumor cells. Primary tumor cells were harvested from diverse clinical tumor tissues from 60 patients (15 \times 4 types) of breast, ovarian, colorectal, and gastric cancers (recruited regardless of their pathological subtypes). Detailed information for the clinical samples is provided in Table S5. Note that we also included immortalized tumorigenic cell lines HeLa and MCF7 (human breast adenocarcinoma cell), and non-tumorigenic cell lines MCF10A (derived from human mammary epithelial cells widely used as normal breast cells) and MRC5 (derived from human normal lung tissue) in these experiments. For the patient tumor materials, we split each tumor mass into three parts for WGS to assess the innate CIN level of tumors, to generate primary tumor cells for *in vitro*

proliferation assays, and to cultivate patient-derived tumor xenografts (PDX) for *in vivo* studies.

By analyzing CIN, we ranked all 60 tumor samples and four immortalized cell lines (64 in total) in descending order based on their intrinsic CIN level (Fig. 4a). Briefly, the eight tumor samples bearing the highest CIN level were CIN1_{COLON}, CIN2_{COLON}, CIN3_{BREAST}, CIN4_{COLON}, CIN5_{OVARY}, CIN6_{GASTRIC}, CIN7_{COLON}, and CIN8_{BREAST}. The eight tumor samples bearing the lowest CIN level were CIN57_{OVARY}, CIN58_{GASTRIC}, CIN59_{COLON}, CIN60_{GASTRIC}, CIN61_{BREAST}, CIN62_{BREAST}, CIN63_{MCF10A}, and CIN64_{MRC5} (Fig. 4a). Accordingly, we tested the expression levels of the top 20 candidate cytokinesis genes in these 16 tumor samples. As expected, most of the 20 genes tended to be highly expressed in high-CIN tumor samples compared with those in low-CIN tumor samples (Figs. 4b, S5, Table S6), although a few genes (PPM1G, SEC61B, and TRIM28) showed no difference between high-CIN and low-CIN groups. In particular, the expression levels of PPP4C and TBCB in CIN1–CIN8 were higher than those in CIN57–CIN64. Western blot of PPP4C and TBCB confirmed the mRNA results across paired samples (CIN1_{COLON} vs. CIN59_{COLON}, CIN3_{BREAST} vs. CIN62_{BREAST}) (Fig. 4c). We selected these 16 samples (eight high-CIN and eight low-CIN) to assess any CIN-dependent differential impacts of PPP4C or TBCB knockdown in a cell proliferation assay using the xCELLigence RTCA system for real-time, non-invasive monitoring of long term cell growth [45,46].

Confirming our supposition about the likely utility of targeting cytokinesis bridge genes, we observed that lentivirus-based shRNA knockdown of PPP4C and TBCB (Fig. S6) significantly suppressed proliferation in all eight of the high-CIN tumor cells compared to their corresponding scramble shRNA controls (Fig. 4d). Specifically, we found that PPP4C knockdown decreased proliferation by around 80% for the CIN1_{COLON} and CIN3_{BREAST} cells by 70 and 50 h, respectively, when their corresponding controls reached a growth plateau. Also, the anti-proliferative effect was observed upon PPP4C knockdown for the six remaining high-CIN cells (reduced proliferation ranging from 50.21% to 78.51%; Fig. 4d). Similarly, TBCB knockdown reduced the proliferation of high-CIN cells by 66.14% on average with the highest reduction of 84.44% compared to their non-knockdown controls (Fig. 4d). In contrast, mild suppression of proliferation was detected upon knockdown of PPP4C or TBCB in the low-CIN cells, including for the immortalized normal cell lines MCF10A and MRC5. The average decrease in proliferation for the low-CIN cells was 23.71% (Fig. 4e). These results for clinical samples from patients with highly diverse cancer types clearly demonstrate that targeting cytokinesis bridge genes PPP4C and TBCB reduces proliferation of high-CIN cancer cells. To facilitate future research on cytokinesis bridge components in our list, we searched and summarized usable inhibitors of all 218 proteins. At least 84 inhibitors against 46 cytokinesis bridge proteins are commercially available or already made by labs (Table S7). These compounds would be convenient tools to mine our list for cancer treatment research.

3.5. Knockdown of cytokinesis bridge genes PPP4C and TBCB induces micronuclei formation and activates cGAS to drive apoptosis

Given the strong anti-proliferative effects upon knockdown of cytokinesis bridge components PPP4C and TBCB, we were curious about the underlying mechanism. Microscopic analysis of live cells labeled with dyes that stain microtubules and nuclei revealed that knockdown of PPP4C or TBCB in high-CIN primary tumor cells prevented most of the cells from completing cytokinesis, caused diverse abnormal chromosome phenotypes, and resulted in production of many micronuclei in cells (Fig. 5a–d, Video S2–7). Specifically, we observed non-segregated chromosomes and chromosome fragments near the cytokinetic bridge, and found abnormal distributions of actin, tripolar division, and asymmetrical cytokinesis in high-CIN cells upon PPP4C or TBCB knockdown (Fig. 5a). The micronuclei formation induced by cytokinesis failure is supported by previous studies [53,54]. The average proportion of these cells exhibiting micronuclei was 69.15%, with the highest rate of 80.7%

in CIN1_{COLON} cells upon PPP4C knockdown (Fig. 5d). In contrast, we found that many fewer low-CIN primary tumor cells (mean percentage of 25.33%) contained micronuclei upon the knockdown of PPP4C or TBCB (Fig. 5a–d).

Micronuclei originate from the mis-segregation of chromosomes during cytokinesis, and these cellular structures contain leaked nuclear chromatin surrounded by their own envelope that directly contributes to CIN [53–55]. Leaked nuclear materials are known to drive the activation of cyclic GMP-AMP synthase (cGAS), a cytosolic sensor of nucleic acids for both inflammation and DNA-damage responses [56,57]. Thus, we examined whether PPP4C and TBCB knockdown may activate the cGAS pathway. We found cGAS activation in high-CIN primary tumor cells upon knockdown, and specifically noted that the aggregated cGAS signal was almost exclusively localized to the micronuclei of tumor cells (Fig. 5e, 5f). Moreover, the cellular level of cGAMP, a 2'-3'-linked cyclic dinucleotide second messenger produced by activated cGAS [57,58], in high-CIN tumor cell groups was significantly higher than that in low-CIN tumor cell groups upon knockdown of PPP4C and TBCB (Fig. 5g). Consistent with the known sequence of signaling events following cGAS activation, we found that knockdown of PPP4C or TBCB in high-CIN primary tumor cells (CIN1_{COLON}) caused phosphorylation-mediated activation of the downstream cGAS target protein stimulator of interferon genes (STING), (Fig. 5h). Moreover, we confirmed that STING subsequently transmitted the cGAS signal to its binding partner interferon regulatory factor 3 (IRF3) (Fig. 5i). Compared to the high-CIN cells, the knockdown-induced response of STING and IRF3 was much reduced in low-CIN cells (CIN62_{BREAST}, since CIN63_{MCF10A} and CIN64_{MRC5} are non-tumorigenic cell lines, we selected CIN62_{BREAST} for pairing with CIN1_{COLON}) (Fig. 5h, 5i).

Immunoblotting against the activated (cleaved) form of the apoptotic executioner protein caspase-3 and fluorescence staining for active apoptosis (kit assay) revealed that knockdown of PPP4C or TBCB in high-CIN primary tumor cells strongly promoted apoptosis, findings which were further confirmed by our analysis of the pro-apoptotic pore-forming protein BCL-2-associated X protein (BAX) (Figs. 5j–l, S7a). When cGAS was jointly knocked down with PPP4C or TBCB in CIN1_{COLON} and CIN62_{BREAST} tumor cells (Fig. S7a), we did not observe phosphorylation of STING or IRF3 in the high-CIN (CIN1_{COLON}) tumor cells (Fig. 5h, 5i). Accordingly, the apoptotic pathway was not activated in these cells (Fig. 5j), confirming the cGAS-STING-apoptosis axis upon PPP4C or TBCB knockdown in high-CIN tumors. Moreover, we noticed that the basal micronuclei percentages and cGAS activity were slightly increased in high-CIN tumor cells compared to low-CIN tumor cells (Fig. 5d, 5f). We in turn examined the basal apoptosis and cell cycle progression in these tumor cells to rule out an extra cell-killing contribution by basal apoptosis and cell cycle inhibition. As seen in Fig. S7a, c and d, the basal apoptosis in high-CIN tumors detected by active apoptosis signal (1.6–5.2% of detected cells) and BAX signal (2.3–5.6% of detected cells) was slightly increased compared with that in low CIN tumors (0.4–3.1% for active apoptosis; 0.9–3.6% for BAX), and basal apoptosis was not substantially promoted.

In parallel, we tested cell cycle progression of these tumor cells by flow cytometry. High-CIN samples showed 33.15–64.57% G1 stage cells, 24.46–44.99% S stage cells, and 10.97–24.51% G2/M stage cells; low-CIN samples showed 33.84–64.81% G1 stage cells, 24.41–45.64% S stage cells, and 10.64–24.53% G2/M stage cells (Fig. S7e). Due to the heterogeneity of tumors from different patients and diverse cancer types, we did not find obvious trends of cell cycle progression across high-CIN and low-CIN tumor samples. These results are consistent with the present understanding of how micronuclei and leaked nuclear materials can drive cGAS pathway activation and apoptosis, and therefore provide a highly plausible explanation for the strong anti-proliferative effects we observed upon knockdown of cytokinesis bridge components PPP4C and TBCB in high-CIN tumor cells from patients with diverse cancers.

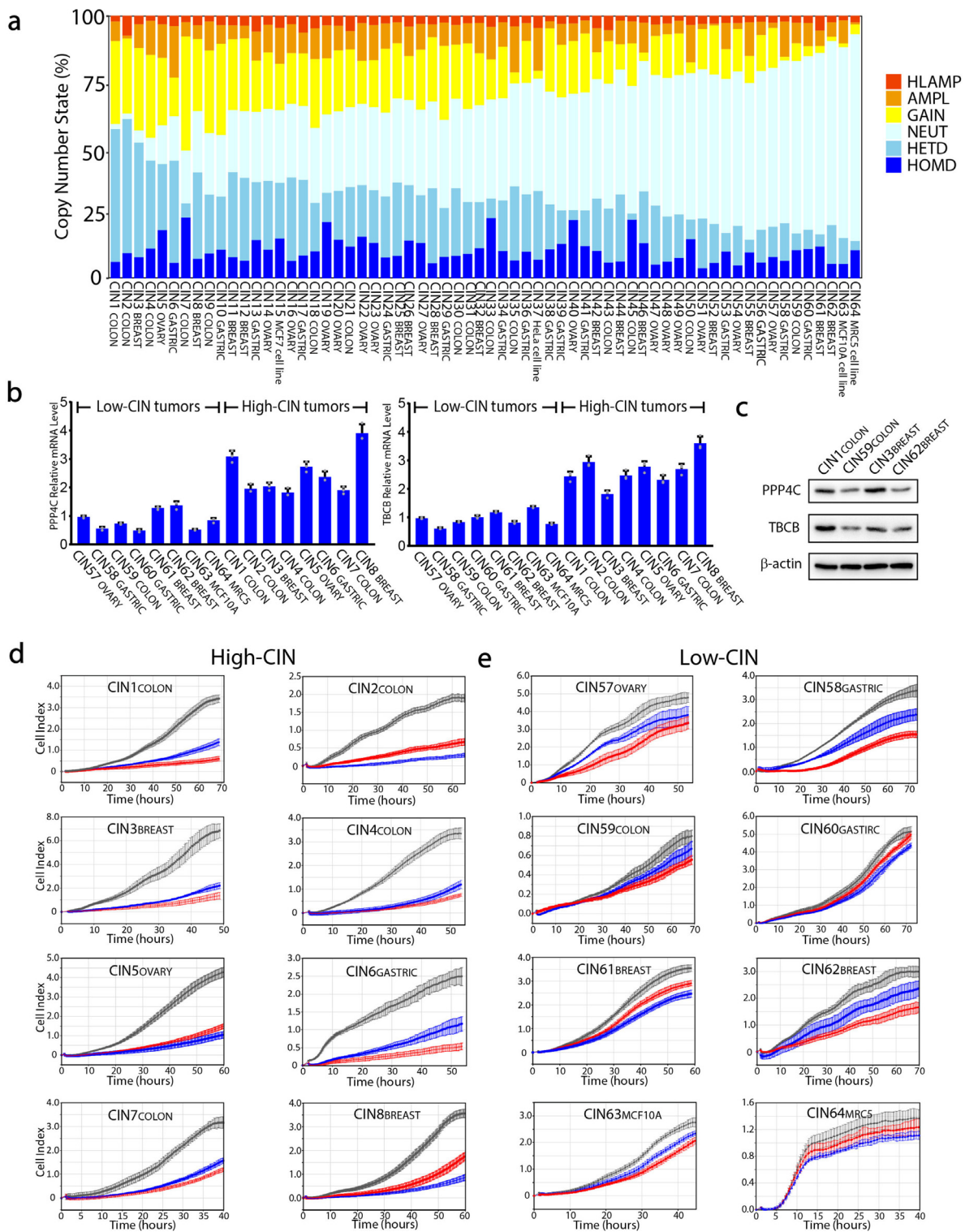


Fig. 4. Suppression of cancer cell proliferation by knockdown of cytokinesis bridge genes. (a) Levels of intrinsic CIN in clinical tumor samples and immortalized cell lines. Intrinsic CIN levels of 60 clinical tumor samples (from 15 breast, 15 ovarian, 15 colorectal, and 15 gastric cancer patients) and four immortalized cell lines (HaLa, MCF7, MCF10A, and MRC5) were assessed using the weighted-genomic integrity index (wGII) in HMMcopy. Segments of specific copy number variation events were classified into six states including homozygous deletion (HOMD), heterozygous deletion (HETD), neutral change (NEUT), gain of chromosome (GAIN), amplification event (AMPL), and high level amplification (HLAMP). CIN levels of different samples were ranked in descending order. (b) mRNA expression levels of PPP4C and TBCB in high-CIN and low-CIN tumor samples analyzed by quantitative PCR. Error bars, mean \pm SD from three independent experiments. (c) Protein expression levels of PPP4C and TBCB in high-CIN (CIN1_{COLON} vs CIN59_{COLON}) and low-CIN tumor (CIN3_{BREAST} vs CIN62_{BREAST}) samples analyzed by western blot. β -actin was used as a loading control. (d, e) Real-time cell proliferation assay of high-CIN and low-CIN tumor cells upon knockdown of PPP4C or TBCB. 5,000-10,000 cells with or without knockdown of PPP4C or TBCB were seeded into 16-well plates and the proliferation was recorded by the xCELLigence RTCA system, which enables real-time, non-invasive monitoring of cell growth dynamics. Cell proliferation for each tumor type was automatically monitored over 40–70 h (i.e. until the control cells for that cell line reached a growth plateau). PPP4C and TBCB knockdown groups are shown by red and blue lines, respectively, and control group treated with scramble shRNA is shown by grey lines. Error bars represent the standard deviation.

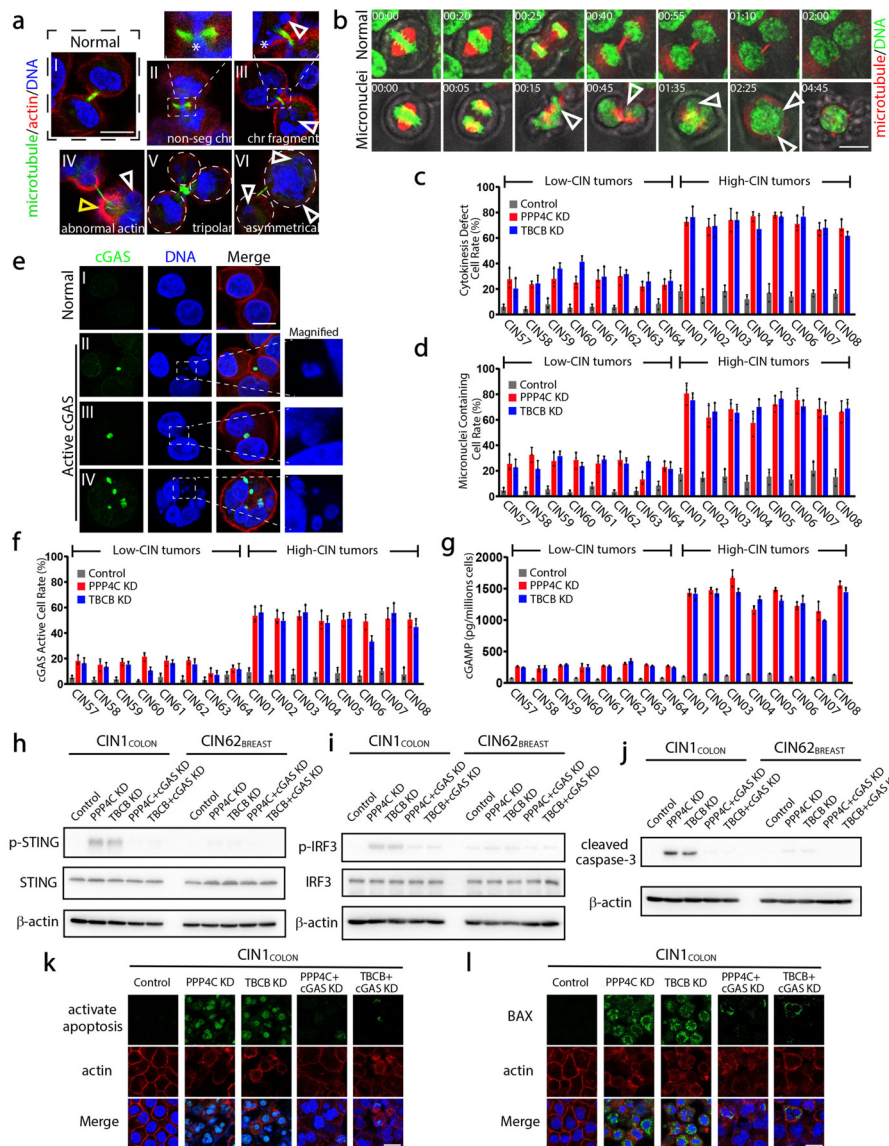


Fig. 5. Knockdown of cytokinesis bridge genes promotes formation of micronuclei and apoptosis. (a) Abnormal cytokinesis of tumor cells upon knockdown of PPP4C or TBCB. A variety of abnormal cytokinesis phenotypes were observed upon shRNA knockdown of PPP4C or TBCB in the eight high-CIN tumor cells. Abnormal cytokinesis phenotypes included micronuclei (white arrowheads, i.e. cell example III from CIN3^{BREAST} tumor cells upon PPP4C knockdown; cell example IV from CIN4^{COLON} tumor cells upon TBCB knockdown; cell example VI from CIN6^{GSATRIC} tumor cells upon TBCB knockdown) and attendant non-segregated chromosomes and chromosome fragmentation at the cytokinetic bridge (asterisks, i.e. cell example II from CIN1^{COLON} tumor cells upon PPP4C knockdown; cell example III from CIN3^{BREAST} tumor cells upon PPP4C knockdown), as well as abnormal actin (yellow arrowhead, i.e. cell example IV from CIN4^{COLON} tumor cells upon TBCB knockdown), tripolar division (dashed circle, i.e. cell example V from CIN5^{OVARY} tumor cells upon TBCB knockdown), and asymmetrical cytokinesis (dashed circle, i.e. cell example VI from CIN6^{GSATRIC} tumor cells upon TBCB knockdown). Normal cytokinesis of cell example I from CIN1^{COLON} tumor cells treated with scramble shRNA. Scale bar, 10 μ m. (b) Real-time imaging of cytokinesis upon PPP4C or TBCB knockdown. Cells that were live labeled against microtubules (cell-permeable taxol-based fluorescent probes) and nuclei (cell-permeable DNA dyes) were monitored with live-imaging. Normal cytokinesis (cell example from CIN1^{COLON} tumor cells treated with scramble shRNA) produces two daughter cells, while the abnormal cytokinesis (cell example from CIN1^{COLON} tumor cells) caused by PPP4C knockdown was characterized by increased numbers of generated micronuclei and frequent apoptosis. Scale bar, 10 μ m. (c) Cytokinesis defect rates of low-CIN and high-CIN cells upon PPP4C or TBCB knockdown. Error bars, mean \pm SD. At least 100 cells in each group from three independent repeats were examined. (d) Micronuclei formation rates for low-CIN and high-CIN cells upon PPP4C or TBCB knockdown. Error bars, mean \pm SD. At least 100 cells in each group from three independent repeats were examined for containing or not containing micronuclei. (e) Immunofluorescence staining revealing cGAS activation in tumor cells upon PPP4C or TBCB knockdown. High-CIN cells featured aggregated cGAS, and the cGAS signal was co-localized with micronuclei in one daughter cell (cell example II from CIN1^{COLON} tumor cells upon PPP4C knockdown), between the separated nuclei of a cell (cell example III from CIN3^{BREAST} tumor cells upon PPP4C knockdown), and in cells with multiple nuclei (cell example IV from CIN5^{OVARY} tumor cells upon TBCB knockdown). Normal (cGAS inactive) cell example I from CIN1^{COLON} tumor cells treated with scramble shRNA. Boxed areas indicate the co-localization of cGAS and micronuclei. Scale bar, 10 μ m. (f) Rates of cGAS activation in the low-CIN and high-CIN cells upon PPP4C or TBCB knockdown. Error bars, the mean \pm SD. At least 100 cells in each group from three independent repeats were examined. (g) Cellular cGAMP level of low-CIN and high-CIN cells upon PPP4C or TBCB knockdown measured by ELISA. Error bars, the mean \pm SD from three independent experiments. (h, i) Activation of STING and IRF3 in high-CIN and low-CIN tumor cells upon single knockdown (PPP4C or TBCB) and double knockdown (PPP4C/cGAS or TBCB/cGAS). Immunoblotting against STING, phosphorylated STING, IRF3, and phosphorylated IRF3 in CIN1^{COLON} (high-CIN) and CIN62^{BREAST} (low-CIN) cells after knockdown of PPP4C or TBCB. β -actin was used as a loading control. (j) Immunoblotting against the activated (cleaved) form of the apoptotic executioner protein caspase-3 in high-CIN (CIN1^{COLON}) and low-CIN (CIN62^{BREAST}) cells after single knockdown (PPP4C or TBCB) and double knockdown (PPP4C/cGAS or TBCB/cGAS). β -actin was used as a loading control. (k, l) Fluorescence staining for activated caspase-3 assay and immunofluorescence staining of pro-apoptotic pore-forming protein BAX in high-CIN (CIN1^{COLON}) and low-CIN (CIN62^{BREAST}) cells after single knockdown (PPP4C or TBCB) and double knockdown (PPP4C/cGAS or TBCB/cGAS). Scale bar, 20 μ m.

3.6. Hitting cytokinesis bridge gene PPP4C kills high-CIN tumors in vivo

To test whether intervening cytokinesis bridge genes can kill high-CIN tumors *in vivo*, we employed a patient-derived tumor xenograft (PDX) model in mice. The highest and lowest CIN samples in breast, ovarian, colorectal, and gastric tumors of patients from Fig. 4a were selected for inoculation for the highest: CIN1_{COLON}, CIN3_{BREAST}, CIN5_{OVARY}, and CIN10_{GASTRIC} (CIN6_{GASTRIC} failed to develop tumors in PDX, so CIN10_{GASTRIC} was used); and lowest: CIN57_{OVARY}, CIN59_{COLON}, CIN60_{GASTRIC}, and CIN62_{BREAST}. Fig. 6a shows the growth curve (blue lines) of the eight PDX tumors of the second generation. We monitored these mice for 40–60 days when all types of tumor seeds developed obvious solid tumors. Generally, high-CIN typed tumors and low-CIN typed tumors did not exhibit significant differences in tumor growth, at least during our observation. On histochemistry, these tumors were actively proliferating based on Ki67 staining, accompanying less apoptosis marked by cleaved caspase-3 (Fig. 6b, 6c). Upon knockdown of PPP4C in PDX tumors by PPP4C-shRNA lentivirus since Day 20 after implantation, we observed significant reduction of all the high-CIN tumors from 30–60 days after implantation. The mean reduced volume of CIN1_{COLON}, CIN3_{BREAST}, CIN5_{OVARY}, and CIN10_{GASTRIC} were 74.1%, 69.8%, 78.7%, and 74.2%, respectively (Fig. 6a). In contrast, no obvious inhibition of tumor growth was found on the low-CIN tumors after PPP4C-shRNA treatment (Fig. 6a).

For immunohistochemistry (IHC), the reduced high-CIN tumor masses contained fewer Ki67 positive cells and showed intensive signals of apoptosis, which was very different from that in the control and low-CIN tumor masses (Fig. 6b, 6c). When testing the status of cGAS, we found significant activation of cGAS in high-CIN tumors but not in low-CIN tumors upon PPP4C knockdown (Fig. 6d, 6e). To further confirm the cGAS-STING-apoptosis axis *in vivo*, we knocked down cGAS in addition to PPP4C in CIN3_{BREAST} PDX mice by shRNA lentivirus since Day 20 after implantation and monitored tumor development. Compared with the shrunken tumors in the PPP4C single knockdown, tumors in the cGAS/PPP4C double knockdown became deteriorated with an increased volume (Fig. S8a). Within tumors detected by IHC, more Ki67 positive cells and fewer apoptotic cells were found in cGAS/PPP4C double knockdown group than in PPP4C knockdown group (Fig. S8b). We attribute the elevated fluorescence signal of cGAS in tissue sections upon the knockdown of PPP4C (Fig. 6d) to a higher level of interferon from the *in vivo* microenvironment of the tumor site than the *in vitro* cultured tumor cells [59,60].

Interferon-simulated gene expression was recently shown to be overactive in micronuclei containing cells [56], and the expression of cGAS could be specifically induced by interferon through two adjacent interferon-sensitive response elements (ISREs) in the cGAS promoter [61]. Accordingly, we measured interferon levels of cultured tumor cells *in vitro* and tumor masses harvested from tumor bearing mice. We found no significant difference of interferon levels between cultured high-CIN (CIN1_{COLON}, CIN3_{BREAST}, CIN5_{OVARY}, CIN10_{GASTRIC}) and low-CIN tumor cells (CIN59_{COLON}, CIN62_{BREAST}, CIN57_{OVARY}, CIN60_{GASTRIC}) upon knockdown of PPP4C. The interferon level was significantly higher in high-CIN tumor tissues than that in low-CIN tumor tissues, accompanying a mild increase of cGAS expression (Fig. S8c–S8e). Together, these data suggest that hitting cytokinesis factor PPP4C effectively suppresses multiple types of high-CIN tumors *in vivo*.

4. Discussion

Current scientific advances have uncovered high heterogeneity of human tumors that sharply decreases therapeutic efficacy in clinic [2,62,63]. Thus, deciphering potential common features of cancer cells is necessary to design and improve treatment strategies. Most tumor cells show CIN to different extents characterized by abnormal chromosomal content [6,64]. Ongoing CIN continually drives karyotypic diversity and allows tumor cells to acquire genetic variations and evolve

[65,66]. Meanwhile, CIN loads stress on tumor cells *per se* that pushes them near collapse. For instance, mammalian cells bearing extra chromosomes have impaired metabolism, proliferation, viability, and fitness [15], and most human trisomy carriers cannot survive [67]. These findings imply a potential survival limitation beyond which cancer cells die because they cannot bear CIN-induced stress [68,69]. However, whether the limitation really exists and how to push cancer cells to break the limitation are unknown. Taking advantage of the engineered peroxidase of APEX2, we established a CB-APEX reaction precisely within the cytokinetic bridges of living, dividing cells and decoded the proteomics of cytokinesis factors. Importantly, we found that elevation of cellular CIN by knockdown of cytokinesis bridge genes can kill diverse types of high-CIN tumors, making this a promising strategy for cancer treatment in the future.

Due to innate traits of CIN, tumor cells have tight regulations for cytokinesis [70]. In our study, 218 high-score proteins were identified in the cytokinetic bridge. For cellular components, these proteins are mainly clustered into ‘chromosomal region’, ‘midbody’, ‘spindle’, ‘focal adhesion’, ‘secretory granule membrane’, ‘nuclear envelope’, and ‘actin cytoskeleton’, (Fig. S2c), suggesting a complicated regulation network for this process. Importantly, when mapping the overall expression patterns of the 218 cytokinesis bridge genes to large numbers of cancer patients in public databases, we found that cancer patients (n=2,376) with high expression of these 218 genes have significantly shorter survival than those (n=2,376) who had low expression, demonstrating that high expression of cytokinesis bridge genes may benefit tumor development. When focusing on individual genes, we found that the high expression trend applies to nearly all types of cancers available in the databases. For example, protein-disulfide isomerase-associated 3 (PDIA3) exhibits dominant high expression across all tumor types such as esophageal carcinoma (ESCA), glioblastoma multiforme (GBM), pancreatic adenocarcinoma (PAAD), skin cutaneous melanoma (SKCM), and stomach adenocarcinoma (STAD).

The high expression of cytokinesis bridge genes is strongly reminiscent of the high expression of spindle pole clustering proteins in tumor cells. Centrosome amplification has been observed in many solid tumors [71,72]. Although in principle centrosome amplification easily causes multipolar spindles that arrest cell cycle, most tumor cells can apparently suppress multipolarity and fulfill their division by overexpressing spindle pole clustering proteins, such as TPX2 and HSET [73,74]. Accordingly, knockdown of signature clustering proteins could cause cluster failure and suppress tumor growth [73,74]. Thus, our results provide a potentially powerful strategy for treating diverse types of cancers by targeting cytokinesis bridge genes. Interestingly, among all analyzable cancer types, only acute myeloid leukemia (AML) patients showed significantly low expression of cytokinesis bridge genes. This may imply an obviously different mechanism of tumor development between solid tumors and leukemia.

Another benefit for targeting cytokinesis against tumors comes from its rapid course as well as it being the final step of the cell cycle. Although cancer cells can correct errors for survival during their life cycle [64], it seems harder to fix abrupt chromosomal aberrations in transient cytokinesis. Therefore, neither the PPP4C nor TBCB knockdown cells in our study (based on our live imaging observation) reversed their failed cytokinesis when the micronuclei had formed and escaped from apoptosis. Micronuclei directly contribute to CIN and DNA damage resulting from nuclear envelope collapse that promptly activates cGAS [53,56]. The rapid response from cytokinesis failure to cGAS-mediated apoptosis (the “cytokinesis failure induced micronuclei (CFM)-cGAS-apoptosis” axis) guarantees the impossibility of self-rescue by cancer cells. Previous studies have found that cGAS suppresses homologous recombination repair of nuclear DNA damage and contributes to genome destabilization, uncovering a novel role of cGAS in tumorigenesis [75,76]. This “pro-tumor” role of cGAS depends on the presence of DNA damages in the nucleus and constant accumulation of these damages for genome instability and then tumorigenesis. The “CFM-cGAS-apoptosis” response in

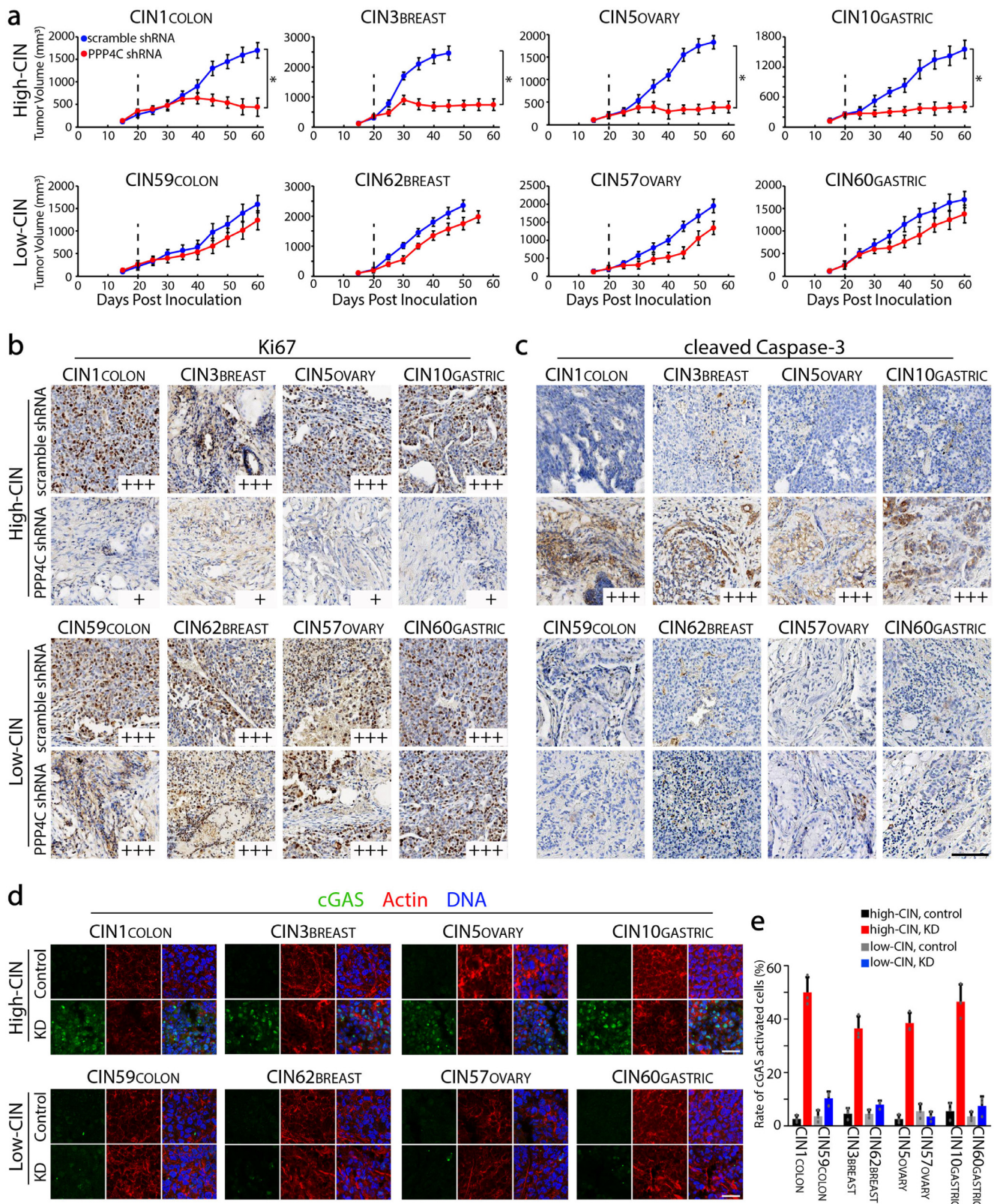


Fig. 6. Killing high-CIN tumors *in vivo* by knockdown of cytokinesis bridge genes. (a) Growth curve of diverse types of tumors in PDX model upon knockdown of cytokinesis bridge gene PPP4C. High-CIN tumors (CIN1_{COLON}, CIN3_{BREAST}, CIN5_{OVARY}, CIN10_{GASTRIC}) and low CIN tumors (CIN59_{COLON}, CIN62_{BREAST}, CIN57_{OVARY}, CIN60_{GASTRIC}) of breast, ovarian, colorectal, and gastric cancer patients were treated with scramble or PPP4C shRNA lentivirus in PDX mice. Dotted line denotes time point of shRNA treatment. Asterisk indicates significant difference between tumor volumes. (b, c) Immunohistochemical staining of Ki67 and cleaved Caspase-3 in high-CIN and low-CIN tumors treated with scramble or PPP4C shRNA lentivirus from PDX mice. Varying number of “+” denotes different levels of positive signal of Ki67 or cleaved Caspase-3 in tumors. Scale bar, 100 μ m. (d) Immunofluorescent staining of cGAS in high-CIN and low CIN tumors treated with scramble or PPP4C shRNA lentivirus from PDX mice. Upon PPP4C downregulation, cGAS was activated in numerous tumor cells in high-CIN tumors, while the activation occurred in sporadic tumor cells in low-CIN tumors. Scale bar, 50 μ m. (e) Percentage of cGAS positive cells from “d” in high-CIN and low CIN tumors treated with scramble or PPP4C shRNA lentivirus from PDX mice. Error bars, mean \pm SD. At least 100 cells in each group from 3–5 independent slides were counted.

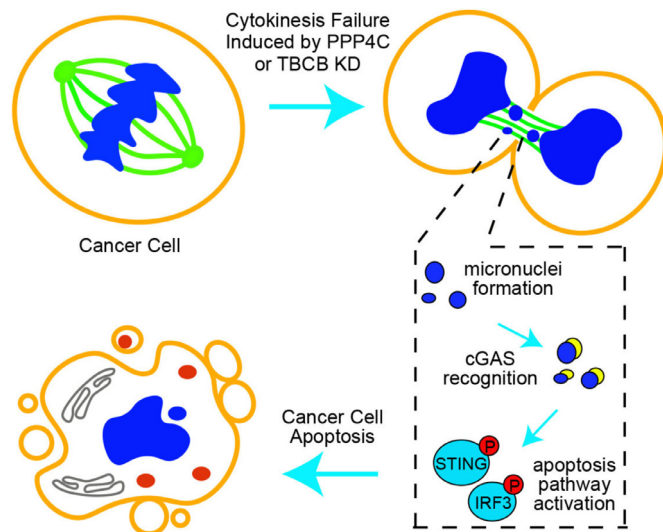


Fig. 7. A model of cancer cell apoptosis induced by the knockdown of cytokinesis genes *PPP4C* and *TBCB*. Cancer cells express high levels of cytokinesis factors such as *PPP4C* and *TBCB* that are required for tight regulation of cytokinesis. The knockdown of *PPP4C* and *TBCB* causes cytokinesis failure leading to micronuclei formation. The micronuclei are recognized by cGAS that activates STING and IRF3 for apoptosis. The activated apoptosis leads to cancer cell death.

our study is triggered by micronuclei formation upon cytokinesis failure during the mitosis of cancer cells, and the micronuclei are quickly recognized by cytosolic cGAS. Since “CFM-cGAS” activates STING and apoptosis, the responding cancer cells tend to die (Fig. 7). Thus, the different roles of cGAS hinge on the upstream events of the cell, nuclear DNA damage, or cytokinesis failure induced micronuclei.

In the confined space of the cytokinetic bridge, besides cytoskeleton associated proteins, various clusters of components such as histone binding proteins are found. The presence of histone binding proteins in the bridge is interesting because it is a further hint of the existence of residual chromosome(s) or DNA in a time window of cytokinesis. Scientists have explored this field since the ‘NoCut’ pathway was identified ten years ago for preventing early cuts in chromosomes during cytokinesis [77,78]. Moreover, manipulations of cell cycle checkpoints are always popular therapeutic approaches against cancers. Unlike checkpoints of G1, S phase, G2/M, or spindle assembly checkpoint in mitosis, no well-recognized checkpoint has been precisely identified in cytokinesis. Our cytokinesis proteome would help to figure out whether a checkpoint system really exists for cytokinesis and what the components are. Lastly, to facilitate future research on cytokinesis proteins, we searched and summarized usable inhibitors (commercially available or already made by labs) of all 218 proteins. At least 84 inhibitors against 46 cytokinesis bridge proteins are available and ready for use, making them convenient tools for mining our proteome resource in the future.

5. Conclusion

This study decodes the cellular proteome of the cytokinetic bridge, a confined space transiently present during cell division, which is unreachable for most conventional proteomic techniques. Elevation of cellular CIN by knockdown of cytokinesis bridge genes such as *PPP4C* and *TBCB* kills diverse types of high-CIN tumors and is a promising strategy for cancer treatment in the future.

Declaration of Competing Interest

The authors declare that they have no known competing financial interests or personal relationships that could have appeared to influence the work reported in this paper.

Acknowledgments

Mass spectrometry experiments were carried out by ZhengDa Health Company (Beijing, China). Whole genome sequencing was carried out by Annoroad Genomics Company (Beijing, China). We thank Dr. Wenchuan Leng for assistance with analysis of mass spectrometry data. This work was supported by the National Natural Science Foundation of China (NSFC) (Grants No. 81672610, 81521002, 81871160) to ML, and by the “Clinic + X” program (to ML) of Peking University.

Supplementary materials

Supplementary material associated with this article can be found, in the online version, at doi:10.1016/j.fmre.2021.08.015.

References

- [1] T.J. Hudson, W. Anderson, A. Artez, et al., International network of cancer genome projects, *Nature* 464 (7291) (2010) 993–998.
- [2] S. Turajlic, A. Sottoriva, T. Graham, et al., Resolving genetic heterogeneity in cancer, *Nat. Rev. Genet.* 20 (7) (2019) 404–416.
- [3] P.K. Ng, J. Li, K.J. Jeong, et al., Systematic functional annotation of somatic mutations in cancer, *Cancer Cell* 33 (3) (2018) 450–462.
- [4] J.R. Mayers, M.E. Torrence, L.V. Danai, et al., Tissue of origin dictates branched-chain amino acid metabolism in mutant Kras-driven cancers, *Science* 353 (6304) (2016) 1161–1165.
- [5] Z. Kan, B.S. Jaiswal, J. Stinson, et al., Diverse somatic mutation patterns and pathway alterations in human cancers, *Nature* 466 (7308) (2010) 869–873.
- [6] D. Hanahan, R.A. Weinberg, Hallmarks of cancer: the next generation, *Cell* 144 (5) (2011) 646–674.
- [7] R.A. Burrell, N. McGranahan, J. Bartek, et al., The causes and consequences of genetic heterogeneity in cancer evolution, *Nature* 501 (7467) (2013) 338–345.
- [8] C.M. Bielski, A. Zehir, A.V. Penson, et al., Genome doubling shapes the evolution and prognosis of advanced cancers, *Nat. Genet.* 50 (8) (2018) 1189–1195.
- [9] S.M. Dewhurst, N. McGranahan, R.A. Burrell, et al., Tolerance of whole-genome doubling propagates chromosomal instability and accelerates cancer genome evolution, *Cancer Discov.* 4 (2) (2014) 175–185.
- [10] T.I. Zack, S.E. Schumacher, S.L. Carter, et al., Pan-cancer patterns of somatic copy number alteration, *Nat. Genet.* 45 (10) (2013) 1134–1140.
- [11] J.M. Schwartzman, R. Sotillo, R. Benezra, Mitotic chromosomal instability and cancer: mouse modelling of the human disease, *Nat. Rev. Cancer* 10 (2) (2010) 102–115.
- [12] E.C. de Bruin, N. McGranahan, R. Mitter, et al., Spatial and temporal diversity in genomic instability processes defines lung cancer evolution, *Science* 346 (6206) (2014) 251–256.
- [13] S.M.A. Lens, R.H. Medema, Cytokinesis defects and cancer, *Nat. Rev. Cancer* 19 (1) (2019) 32–45.
- [14] S.L. Carter, A.C. Eklund, I.S. Kohane, et al., A signature of chromosomal instability inferred from gene expression profiles predicts clinical outcome in multiple human cancers, *Nat. Genet.* 38 (9) (2006) 1043–1048.
- [15] B.R. Williams, V.R. Prabhu, K.E. Hunter, et al., Aneuploidy affects proliferation and spontaneous immortalization in mammalian cells, *Science* 322 (5902) (2008) 703–709.
- [16] E.M. Torres, B.R. Williams, A. Amon, Aneuploidy: cells losing their balance, *Genetics* 179 (2) (2008) 737–746.
- [17] E.M. Torres, T. Sokolsky, C.M. Tucker, et al., Effects of aneuploidy on cellular physiology and cell division in haploid yeast, *Science* 317 (5840) (2007) 916–924.
- [18] S.F. Bakhoun, D.A. Compton, Chromosomal instability and cancer: a complex relationship with therapeutic potential, *J. Clin. Investig.* 122 (4) (2012) 1138–1143.
- [19] Y.C. Tang, B.R. Williams, J.J. Siegel, et al., Identification of aneuploidy-selective antiproliferation compounds, *Cell* 144 (4) (2011) 499–512.
- [20] B. Lacroix, A.S. Maddox, Cytokinesis, ploidy and aneuploidy, *J. Pathol.* 226 (2) (2012) 338–351.
- [21] A. Echard, G.R. Hickson, E. Foley, et al., Terminal cytokinesis events uncovered after an RNAi screen, *Curr. Biol.* 14 (18) (2004) 1685–1693.
- [22] P.J. Thul, L. Akesson, M. Wiking, et al., A subcellular map of the human proteome, *Science* 356 (6340) (2017).
- [23] U.S. Eggert, T.J. Mitchison, C.M. Field, Animal cytokinesis: from parts list to mechanisms, *Annu. Rev. Biochem.* 75 (2006) 543–566.
- [24] P. Bieling, I.A. Telley, T. Surrey, A minimal midzone protein module controls formation and length of antiparallel microtubule overlaps, *Cell* 142 (3) (2010) 420–432.
- [25] T.D. Pollard, B. O’Shaughnessy, Molecular mechanism of cytokinesis, *Annu. Rev. Biochem.* 88 (2019) 661–689.
- [26] T.D. Pollard, Nine unanswered questions about cytokinesis, *J. Cell Biol.* 216 (10) (2017) 3007–3016.

- [27] R.A. Green, E. Paluch, K. Oegema, Cytokinesis in animal cells, *Annu. Rev. Cell Dev. Biol.* 28 (2012) 29–58.
- [28] H.W. Rhee, P. Zou, N.D. Udeshi, et al., Proteomic mapping of mitochondria in living cells via spatially restricted enzymatic tagging, *Science* 339 (6125) (2013) 1328–1331.
- [29] S. Markmiller, S. Soltanich, K.L. Server, et al., Context-dependent and disease-specific diversity in protein interactions within stress granules, *Cell* 172 (3) (2018) 590–604e13.
- [30] V. Hung, P. Zou, H.W. Rhee, et al., Proteomic mapping of the human mitochondrial intermembrane space in live cells via ratiometric APEX tagging, *Mol. Cell* 55 (2) (2014) 332–341.
- [31] B. Schwanhauser, D. Busse, N. Li, et al., Global quantification of mammalian gene expression control, *Nature* 473 (7347) (2011) 337–342.
- [32] Z. Tang, B. Kang, C. Li, et al., GEPIA2: an enhanced web server for large-scale expression profiling and interactive analysis, *Nucleic Acids Res.* 47 (W1) (2019) W556–W560.
- [33] Y. Liao, J. Wang, E.J. Jaehnig, et al., WebGestalt 2019: gene set analysis toolkit with revamped UIs and APIs, *Nucleic Acids Res.* 47 (W1) (2019) W199–W205.
- [34] H. Lui, J. Zhang, S.R. Makinson, et al., Progranulin deficiency promotes circuit-specific synaptic pruning by microglia via complement activation, *Cell* 165 (4) (2016) 921–935.
- [35] B. Xie, L. Zhang, H. Zhao, et al., Poly(ADP-ribose) mediates asymmetric division of mouse oocyte, *Cell Res.* 28 (4) (2018) 462–475.
- [36] H. Li, R. Durbin, Fast and accurate short read alignment with Burrows-Wheeler transform, *Bioinformatics* 25 (14) (2009) 1754–1760.
- [37] H. Li, B. Handsaker, A. Wysoker, et al., The sequence alignment/map format and SAMtools, *Bioinformatics* 25 (16) (2009) 2078–2079.
- [38] A. McKenna, M. Hanna, E. Banks, et al., The genome analysis toolkit: a MapReduce framework for analyzing next-generation DNA sequencing data, *Genome Res.* 20 (9) (2010) 1297–1303.
- [39] K. Wang, M. Li, H. Hakonarson, ANNOVAR: functional annotation of genetic variants from high-throughput sequencing data, *Nucleic Acids Res.* 38 (16) (2010) e164.
- [40] S.F. Bakhoun, B. Ngo, A.M. Laughney, et al., Chromosomal instability drives metastasis through a cytosolic DNA response, *Nature* 553 (7689) (2018) 467–472.
- [41] R.A. Burrell, S.E. McClelland, D. Endesfelder, et al., Replication stress links structural and numerical cancer chromosomal instability, *Nature* 494 (7438) (2013) 492–496.
- [42] S.P. Shah, A. Roth, R. Goya, et al., The clonal and mutational evolution spectrum of primary triple-negative breast cancers, *Nature* 486 (7403) (2012) 395–399.
- [43] E. Talevich, A.H. Shain, T. Botton, et al., CNVkit: genome-wide copy number detection and visualization from targeted DNA sequencing, *PLoS Comput. Biol.* 12 (4) (2016) e1004873.
- [44] S.P. Shah, X. Xuan, R.J. DeLeeuw, et al., Integrating copy number polymorphisms into array CGH analysis using a robust HMM, *Bioinformatics* 22 (14) (2006) e431–e439.
- [45] N. Al Nakouzi, C.K. Wang, E. Beraldi, et al., Clusterin knockdown sensitizes prostate cancer cells to taxane by modulating mitosis, *EMBO Mol. Med.* 8 (7) (2016) 761–778.
- [46] J.L. Heinecke, L.A. Ridnour, R.Y. Cheng, et al., Tumor microenvironment-based feed-forward regulation of NOS2 in breast cancer progression, *Proc. Natl. Acad. Sci. USA* 111 (17) (2014) 6323–6328.
- [47] S.S. Lam, J.D. Martell, K.J. Kamer, et al., Directed evolution of APEX2 for electron microscopy and proximity labeling, *Nat. Methods* 12 (1) (2015) 51–54.
- [48] V. Hung, N.D. Udeshi, S.S. Lam, et al., Spatially resolved proteomic mapping in living cells with the engineered peroxidase APEX2, *Nat. Protoc.* 11 (3) (2016) 456–475.
- [49] C. Hutter, J.C. Zenklusen, The cancer genome atlas: creating lasting value beyond its data, *Cell* 173 (2) (2018) 283–285.
- [50] G.T. Consortium, Human genomics. The genotype-tissue expression (GTEx) pilot analysis: multitissue gene regulation in humans, *Science* 348 (6235) (2015) 648–660.
- [51] S. Turajlic, H. Xu, K. Litchfield, et al., Deterministic evolutionary trajectories influence primary tumor growth: TRACERx renal, *Cell* 173 (3) (2018) 595–610e11.
- [52] A. Janssen, M. van der Burg, K. Szuhai, et al., Chromosome segregation errors as a cause of DNA damage and structural chromosome aberrations, *Science* 333 (6051) (2011) 1895–1898.
- [53] E.M. Hatch, A.H. Fischer, T.J. Deerincq, et al., Catastrophic nuclear envelope collapse in cancer cell micronuclei, *Cell* 154 (1) (2013) 47–60.
- [54] C.Z. Zhang, A. Spektor, H. Cornils, et al., Chromothripsis from DNA damage in micronuclei, *Nature* 522 (7555) (2015) 179–184.
- [55] K. Crasta, N.J. Ganem, R. Dagher, et al., DNA breaks and chromosome pulverization from errors in mitosis, *Nature* 482 (7383) (2012) 53–58.
- [56] K.J. Mackenzie, P. Carroll, C.A. Martin, et al., cGAS surveillance of micronuclei links genome instability to innate immunity, *Nature* 548 (7668) (2017) 461–465.
- [57] A. Ablasser, M. Goldeck, T. Cavlar, et al., cGAS produces a 2'-5'-linked cyclic dinucleotide second messenger that activates STING, *Nature* 498 (7454) (2013) 380–384.
- [58] P. Gao, M. Ascano, Y. Wu, et al., Cyclic [G(2',5')pA(3',5')p] is the metazoan second messenger produced by DNA-activated cyclic GMP-AMP synthase, *Cell* 153 (5) (2013) 1094–1107.
- [59] L. Zitvogel, L. Galluzzi, O. Kepp, et al., Type I interferons in anticancer immunity, *Nat. Rev. Immunol.* 15 (7) (2015) 405–414.
- [60] A. Sistigu, T. Yamazaki, E. Vacchelli, et al., Cancer cell-autonomous contribution of type I interferon signaling to the efficacy of chemotherapy, *Nat. Med.* 20 (11) (2014) 1301–1309.
- [61] F. Ma, B. Li, S.Y. Liu, et al., Positive feedback regulation of type I IFN production by the IFN-inducible DNA sensor cGAS, *J. Immunol.* 194 (4) (2015) 1545–1554.
- [62] I. Dagogo-Jack, A.T. Shaw, Tumour heterogeneity and resistance to cancer therapies, *Nat. Rev. Clin. Oncol.* 15 (2) (2018) 81–94.
- [63] J. Wagner, M.A. Rapsomaniki, S. Chevrier, et al., A single-cell atlas of the tumor and immune ecosystem of human breast cancer, *Cell* 177 (5) (2019) 1330–1345e18.
- [64] V. Archambault, D.M. Glover, Polo-like kinases: conservation and divergence in their functions and regulation, *Nat. Rev. Mol. Cell Biol.* 10 (4) (2009) 265–275.
- [65] A. Targa, G. Rancati, Cancer: a CINful evolution, *Curr. Opin. Cell Biol.* 52 (2018) 136–144.
- [66] C. Lengauer, K.W. Kinzler, B. Vogelstein, Genetic instability in colorectal cancers, *Nature* 386 (6625) (1997) 623–627.
- [67] T.J. Hassold, P.A. Jacobs, Trisomy in man, *Annu. Rev. Genet.* 18 (1984) 69–97.
- [68] A.J. Holland, D.W. Cleveland, Losing balance: the origin and impact of aneuploidy in cancer, *EMBO Rep.* 13 (6) (2012) 501–514.
- [69] I. Vitale, G. Manic, L. Senovilla, et al., Karyotypic aberrations in oncogenesis and cancer therapy, *Trends Cancer* 1 (2) (2015) 124–135.
- [70] D. Gisselsson, Y. Jin, D. Lindgren, et al., Generation of trisomies in cancer cells by multipolar mitosis and incomplete cytokinesis, *Proc. Natl. Acad. Sci. USA* 107 (47) (2010) 20489–20493.
- [71] A.B. D'Assoro, W.L. Lingle, J.L. Salisbury, Centrosome amplification and the development of cancer, *Oncogene* 21 (40) (2002) 6146–6153.
- [72] G. Sluder, J.J. Nordberg, The good, the bad and the ugly: the practical consequences of centrosome amplification, *Curr. Opin. Cell Biol.* 16 (1) (2004) 49–54.
- [73] B. Leber, B. Maier, F. Fuchs, et al., Proteins required for centrosome clustering in cancer cells, *Sci. Transl. Med.* 2 (33) (2010) 33ra38.
- [74] M. Kwon, S.A. Godinho, N.S. Chandhok, et al., Mechanisms to suppress multipolar divisions in cancer cells with extra centrosomes, *Genes Dev.* 22 (16) (2008) 2189–2203.
- [75] H. Jiang, X. Xue, S. Panda, et al., Chromatin-bound cGAS is an inhibitor of DNA repair and hence accelerates genome destabilization and cell death, *EMBO J.* 38 (21) (2019) e102718.
- [76] H. Liu, H. Zhang, X. Wu, et al., Nuclear cGAS suppresses DNA repair and promotes tumorigenesis, *Nature* 563 (7729) (2018) 131–136.
- [77] C. Norden, M. Mendoza, J. Dobbelaere, et al., The NoCut pathway links completion of cytokinesis to spindle midzone function to prevent chromosome breakage, *Cell* 125 (1) (2006) 85–98.
- [78] P. Steigemann, C. Wurzenberger, M.H. Schmitz, et al., Aurora B-mediated abscission checkpoint protects against tetraploidization, *Cell* 136 (3) (2009) 473–484.



Bingteng Xie obtained his PhD degree in Life Science from Northeast Agricultural University of China in 2015. He is now a Postdoctor at Peking University Third Hospital. His major research interest focuses on molecular and proteomic biology of tumorigenesis.



Mo Li is a Professor at Center for Reproductive Medicine, Department of Obstetrics and Gynecology, Peking University Third Hospital, and Deputy Director of National Clinical Research Center for Obstetrics and Gynecology (Peking University Third Hospital). His research area focuses on molecular mechanism and therapeutic strategy of breast and ovarian cancers.